

# Earth and Space Science

## RESEARCH ARTICLE

10.1029/2022EA002430

### Key Points:

- Using Routine Off-nadir Targeted Observations (ROTOs) of Mars Odyssey, we acquire directional thermal infrared (TIR) spectra of the surface
- TIR spectral slopes from the ROTO data enable extraction of sub-pixel anisothermal heterogeneities at fine spatial scales
- A thermal inertia mixing model is used to quantify sub-pixel temperature mixing produced by a checkerboard mixing of surface units

### Correspondence to:

B. E. McKeeby,  
bem101@pitt.edu

### Citation:

McKeeby, B. E., Ramsey, M. S., Tai Udovicic, C. J., Haberle, C., & Edwards, C. S. (2022). Quantifying sub-meter surface heterogeneity on Mars using off-axis Thermal Emission Imaging System (THEMIS) data. *Earth and Space Science*, 9, e2022EA002430. <https://doi.org/10.1029/2022EA002430>

Received 16 MAY 2022

Accepted 3 AUG 2022

### Author Contributions:

**Conceptualization:** B. E. McKeeby, M. S. Ramsey

**Formal analysis:** B. E. McKeeby

**Funding acquisition:** M. S. Ramsey

**Investigation:** B. E. McKeeby

**Methodology:** B. E. McKeeby, M. S. Ramsey, C. J. Tai Udovicic, C. Haberle, C. S. Edwards

**Software:** C. J. Tai Udovicic, C. Haberle, C. S. Edwards

**Supervision:** M. S. Ramsey

**Writing – original draft:** B. E. McKeeby

**Writing – review & editing:** B. E. McKeeby, M. S. Ramsey, C. J. Tai

Udovicic, C. S. Edwards

© 2022 The Authors.

This is an open access article under the terms of the [Creative Commons Attribution-NonCommercial License](https://creativecommons.org/licenses/by-nc/4.0/), which permits use, distribution and reproduction in any medium, provided the original work is properly cited and is not used for commercial purposes.

## Quantifying Sub-Meter Surface Heterogeneity on Mars Using Off-Axis Thermal Emission Imaging System (THEMIS) Data

B. E. McKeeby<sup>1</sup> , M. S. Ramsey<sup>1</sup> , C. J. Tai Udovicic<sup>2</sup> , C. Haberle<sup>2</sup>, and C. S. Edwards<sup>2</sup> 

<sup>1</sup>Department of Geology and Environmental Science, University of Pittsburgh, Pittsburgh, PA, USA, <sup>2</sup>Department of Astronomy and Planetary Science, Northern Arizona University, Flagstaff, AZ, USA

**Abstract** Surface heterogeneities below the spatial resolution of thermal infrared (TIR) instruments result in anisothermality and can produce emissivity spectra with negative slopes toward longer wavelengths. Sloped spectra arise from an incorrect assumption of either a uniform surface temperature or a maximum emissivity during the temperature-emissivity separation of radiance data. Surface roughness and lateral mixing of different sub-pixel surface units result in distinct spectral slopes with magnitudes proportional to the degree of temperature mixing. Routine Off-nadir Targeted Observations (ROTO) of the Thermal Emission Imaging Spectrometer (THEMIS) are used here for the first time to investigate anisothermality below the spatial resolution of THEMIS. The southern flank of Apollinaris Mons and regions within the Medusae Fossae Formation are studied using THEMIS ROTO data acquired just after local sunset. We observe a range of sloped TIR emission spectra dependent on the magnitude of temperature differences within a THEMIS pixel. Spectral slopes and wavelength-dependent brightness temperature differences are forward-modeled for a series of two-component surfaces of varying thermal inertia values. Our results imply that differing relative proportions of rocky and unconsolidated surface units are observed at each ROTO viewing geometry and suggest a local rock abundance six times greater than published results that rely on nadir data. High-resolution visible images of these regions indicate a mixture of surface units from boulders to dunes, providing credence to the model.

**Plain Language Summary** Orbital thermal infrared (TIR) spectral and temperature data are used to determine numerous planetary surface properties, providing insight into how the planet's surface has evolved. This paper applies a new methodology to examine temperature mixing of surfaces with different units and particle sizes (i.e., rock and dust). Using the Thermal Emission Imaging Spectrometer (THEMIS) TIR data at 100 m/pixel, we model emissivity spectra and surface temperature to derive the abundance of these different surface units. TIR spectra are sensitive to sub-pixel temperature differences at small scales. Surfaces with various components heat and cool at differing rates creating temperature differences within each pixel. The extracted TIR spectra will have a negative slope proportional to the degree of the temperature difference. Using a series of post-sunset TIR images from different viewing angles, we model the surface temperature and spectral slope to derive the percent of surface units present. Matching these results to our observations allows for determining each component's particle size and abundance. Additionally, this method creates a thermophysical model that predicts a rock abundance six times greater than models derived from nadir viewing observations. This is critical for understanding modern surface evolution and future exploration, such as landing site selection.

## 1. Introduction

Thermal infrared (TIR) observations of Mars by the multispectral Thermal Emission Imaging System (THEMIS) are used to determine a wide array of surface and atmospheric properties, including surface mineralogy, rock abundance, and thermophysical characteristics, as well as atmospheric dust and water ice contents (Ahern et al., 2021; Bandfield, 2009; Bandfield & Edwards, 2008; Bandfield et al., 2004; Christensen et al., 2003, 2004; Fergason et al., 2006; Hamilton & Christensen, 2005; Putzig et al., 2005; Rodgers et al., 2005; M. D. Smith et al., 2003). Accurate determination of these properties is fundamental to understanding the planet's past and current surface evolution. For example, correct retrieval of the temperature-independent spectral property of emissivity is key to determining surface mineralogy and composition (Bandfield et al., 2004). However, this can require the removal of temperature-mixing effects, which may impart unwanted spectral slopes. Commonly, this involves an assumption of an isothermal pixel-integrated surface temperature within the instrument's instantaneous field of view (IFOV). However, if the corresponding area on the ground contains a surface with units

of differing thermal inertias (TI), the assumption of a uniform surface temperature becomes invalid. This can produce an artificial spectral slope that may complicate future compositional analysis. The minimum fraction at which this occurs is currently unknown. However, in general, the greater the temperature distribution, the more prominent these effects appear in the TIR data.

This work combines an off-nadir THEMIS IR data set, collected by Routine Off-nadir Targeted Observations (ROTOs) of the Mars Odyssey spacecraft, with the KRC thermophysical model (Kieffer, 2013) to describe sub-pixel surface units found in the Apollinaris Mons region. Using KRC, we forward model the effects of anisothermality by way of a two-component surface model using units of differing TI mixed laterally. TIR spectra are sensitive to the degree to which a surface unit remains thermally isolated. This scale is estimated based on the surface's derived TI, obtained from the THEMIS Quantitative TI Mosaic (Bandfield & Edwards, 2008; Ferguson et al., 2006).

Due to their unique viewing geometries, we propose that ROTOs allow for a more accurate determination of sub-pixel thermophysical properties than traditional methods, especially in regions heavily mantled by dust. For example, in dusty environments, the high emission angles achieved by ROTOs permit the THEMIS IFOV to observe the less dusty sides of rocks. In contrast, nadir observations only perceive the dust-mantled tops. The difference in temperature between low TI dust and high TI rock produces sub-pixel anisothermality that, if successfully modeled, can be used to derive a local rock abundance. Determining the particle size is possible where differences in derived TI values result in temperature separability. The work presented here explores derived TI values ranging from 50 to 2,500 thermal inertia units (TIU), corresponding to particle sizes ranging from dust to bedrock, respectively.

## 2. Background

### 2.1. Thermal Inertia

TI describes an object's response to temperature change by storing and losing heat and is controlled by the material's physical properties. Expressed in  $\text{J m}^{-2} \text{K}^{-1} \text{s}^{-1/2}$  or TIU, TI is defined as the square root of the product of conductivity ( $k$ ), density ( $\rho$ ), and specific heat capacity ( $c$ ). TI depends solely on the material itself and is not affected by the latitude, local time, or season. Derived from TIR observations combined with thermophysical models, TI is extensively used to investigate the surface properties of planetary bodies, including Mars (Ahern et al., 2021; Chase et al., 1978; Edwards et al., 2018; Ferguson et al., 2006; Kieffer, 2013; Mellon et al., 2000; Putzig & Mellon, 2007), the Moon (Hayne et al., 2017; Vasavada et al., 2012; Williams et al., 2017), Mercury (Chase et al., 1974; Hiesinger et al., 2020; Morrison, 1970), and Phobos (N. M. Smith et al., 2018). However, interpretation of TI can prove complicated due to the complexity of various mixing scenarios (homogenous surface, checkerboard mixing, and vertical layering). Additionally, in-situ surface investigations demonstrate that more than one material is commonly exposed at the surface (Nowicki & Christensen, 2007). A material's diurnal temperature curve is typically asymmetrical as its temperature tends to peak in the early afternoon and dissipate at night. Where that curve represents mixtures of different TI units, the shape and amplitude of the curve is impacted depending on the relative proportions of those units, their vertical or lateral mixing, and their individual thermophysical properties (Ahern et al., 2021; Nowicki & Christensen, 2007). Separability of mixed component surfaces with different TI values is possible using TIR spectral data, but only if the temperature contrast between the units is significant (Cowart & Rogers, 2021). Here we employ a series of THEMIS ROTO images captured just after sunset and attribute the observed anisothermal spectra to the sub-pixel mixing of surface units with differing TI values.

### 2.2. Thermal Mixing and Emissivity

TIR spectra are sensitive to thermal mixing on a broad range of scales, including those at or below the spatial resolution of current orbital instruments. The TI, albedo, and roughness at scales from micrometers to meters, combined with the incident solar radiation, determine the kinetic temperature of the surface, independent of its composition. However, the derived pixel-integrated brightness temperature (BT) varies as a function of wavelength and degree of sub-pixel temperature mixing. For example, the viewing geometry combined with a mixed temperature surface will result in a different pixel-integrated temperature compared to the same surface viewed at nadir (Bandfield et al., 2015). Surfaces containing sub-pixel mixtures of materials of differing TI typically show

variable (anisothermal) surface temperatures, and the combined radiance from objects of different temperatures no longer matches that of a single blackbody radiance spectrum (Ahern et al., 2021; Cowart & Rogers, 2021; Jakosky, 1978; Nowicki & Christensen, 2007). Here we refer to this as sub-pixel anisothermality.

Changes in the measured emitted radiance from varying emission angles can accentuate this sub-pixel anisothermality, as opposed to other potential causes such as an incorrect assumption of the maximum emissivity (e.g., Bandfield & Edwards, 2008; Bandfield et al., 2015; Osterloo et al., 2008). For example, nearly all silicate phases exhibit near-unit emissivity at some point in the THEMIS wavelength range, however, some chloride salts have emissivity values much less than 1.0 (Lane & Christensen, 1998; Osterloo et al., 2008). Where this occurs and an assumption of 1.0 is used to separate the temperature and emissivity, the target temperature is underestimated, and a negatively sloped emission spectrum results (Bandfield, 2009; Osterloo et al., 2008; Ruff et al., 1997). However, variations in viewing geometry or observing conditions of these “graybody” surfaces do not change the magnitude of spectral slopes, unlike in an anisothermal surface, where the spectral slope variability is a function of temperature mixing at a particular viewing geometry (Bandfield, 2009).

Where sub-pixel anisothermality occurs within an instrument's field of view, the surface no longer behaves in a Planck-like manner with respect to wavelength and temperature. Instead, the Planck radiance function can only match the measured radiance at a single wavelength. Therefore, the standard temperature/emissivity separation analysis is flawed, as it relies on the assumption of a homogenous pixel temperature. This results in an emission spectrum with negatively trending slopes towards longer wavelengths that may complicate subsequent compositional analysis (Bandfield, 2009; Bandfield et al., 2015; Rose et al., 2014). Our work utilizes specialized instrument pointing angles acquired close in time to maximize off-nadir viewing. At off-nadir emission angles, surface anisothermality varies as THEMIS observes different surface units at differing relative proportions. To replicate the various solar illumination conditions achieved by off-nadir viewing would require multiple nadir observations collected at various seasonal and local solar times (Bandfield, 2009; Bandfield & Edwards, 2008). However, this alternative method comes with the added complication of surface and atmospheric changes that may occur between nadir observations.

Due to the sensitivity of the TIR spectrum to thermal mixing below the pixel scale, directional emission measurements provide a unique way to retrieve thermophysical properties (Bandfield & Edwards, 2008). The sub-pixel anisothermal effects on the TIR spectrum are directly proportional to the degree and distribution of macro-scale roughness or the relative proportions of different surface units in each pixel. For example, surfaces with greater degrees of sub-pixel anisothermality exhibit a greater magnitude of negative spectral slopes than isothermal surfaces (Bandfield, 2009; Bandfield & Edwards, 2008; Bandfield et al., 2015; McKeeby & Ramsey, 2020, 2021).

### 2.3. Thermal Mixing and Brightness Temperature

Depending on the target's season, time of day, and latitudinal location, the surface will be colder than the atmosphere. Where this occurs, atmospheric emission is more significant relative to surface emission (Cowart & Rogers, 2021). Atmospheric emission limits the usability of emissivity over the full THEMIS spectral range due to the inability to perform a complete radiance correction (Bandfield et al., 2004). This is the case with many recent THEMIS data acquisitions collected at or near local sunset. In place of emissivity, pixel-integrated BT, derived at wavelengths least affected by the atmosphere, can be used as a proxy to assess the degree of surface thermal mixing. Like emissivity, BT is controlled by surface roughness, local true solar times (LTST), solar longitude ( $L_s$ ), TI, and albedo. Additionally, it assumes a wavelength-dependent Planck-like emission and therefore has a negative slope for anisothermality surfaces for the same reasons as the sloped emissivity spectra.

### 2.4. ROTO Description

ROTO by the Mars Odyssey spacecraft have been used to provide off-nadir viewing of the Martian surface since the second extended mission. The THEMIS IR focal plane consists of 320 cross-track pixels and 240 down-track pixels with 10 ~ 1  $\mu\text{m}$  bandwidth strip filters (Christensen et al., 2004). This has assisted in TIR data acquisition of hard to image targets (e.g., polar regions), as well as studies into atmospheric properties using limb measurements, and imaging of the Martian moons (Phobos and Deimos; Bandfield et al., 2018). Where applied to surface investigations, ROTO data provide a unique view and measure of TIR radiance at varying emission angles within a relatively short acquisition window. For thermophysical studies, ROTO data are typically collected over

**Table 1**  
*Data-Specific Parameters of the Eight Routine off-Nadir Targeted Observation Images Acquired for This Study*

THEMIS Image ID	Roll angle (°)	Emission angle (°)	Solar longitude ( $L_s$ ) (°)	Local time (true) (hr)
186177001	-31	35.3	47.0	18.2
186202001	-24	27.2	47.9	18.3
185939006	-12	13.4	38.3	18.3
185964009	-2	2.6	39.2	18.4
185989005	8	10.2	40.2	18.5
186014012	18	20.3	41.1	18.6
186039007	26	29.4	42.0	18.6
186064009	33	37.5	42.9	18.7

2 weeks allowing near-identical surface footprints to be imaged at differing emission angles and under similar LTST,  $L_s$ , and atmospheric conditions. In the evening, Odyssey's orbit runs from north to south, therefore a positive roll maneuver corresponds to shifting the image cross-track from nadir, corresponding to an eastward shift in the descending orbital images. This provides an excellent opportunity for the analysis and modeling of anisothermal spectral effects. The first ROTO sequence designed specifically to investigate surface roughness was performed in September 2017 and covered a region within Daedalia Planum centered at 237.62°E and -23.26°N. This area contains a unique set of lava flows that display atypical THEMIS thermophysical properties recorded during daytime and nighttime overpasses (Crown & Ramsey, 2017; Simurda et al., 2019).

### 3. Methodology

#### 3.1. Study Location

Apollinaris Mons is a volcanic edifice located between the northern lowland and southern highlands. It covers an area ~190 km wide and features a large summit caldera and ~140 km fan deposit extending to the southeast (Chuang et al., 2019; El-Maarry et al., 2014; Greeley & Spudis, 1981; Robinson et al., 1993). A series of eight new ROTO observations were collected from 18:00 to 19:00 hr LTST, 38°–47°  $L_s$ , 93°–102° solar incidence, and surface emission angles from -31° to +33° (Table 1). Images are centered around 174.26°E, -6.40°N and cover an area that includes the Apollinaris Mons caldera. The ROTO footprint extends north into the lower Medusae Fossae formation and south toward Gusev Crater (Figure 1). This ROTO campaign was specifically designed to investigate the surfaces' thermophysical properties. Apollinaris Mons was chosen due to the documented presence of rough surface features (Bandfield, 2009; Zimbelman & Griffin, 2010) as well as the contested formation hypothesis of the Medusae Fossae Formation (MFF; Bradley et al., 2002; Edgett et al., 1997; Hynes et al., 2003; Mandt et al., 2008; Tanaka, 2000).

We selected two study areas within the THEMIS ROTO data that exhibit warm pixel temperatures (>185 K). A rigorous spectral and thermophysical analysis was performed to quantify the degree of subpixel thermal mixing due to variable surface units. Study area 1 is best described as a warm slope associated with a collapse feature in the lower Medusae Fossae formation, just north of the Apollinaris Mons complex (Figure 2).

The MFF is a large, equatorially located, Amazonian age, fine-grained deposit stretching from 170 to 240°E. Morphological characteristics within the MFF include yardang fields, collapse features, and layered deposits analogous to large terrestrial ignimbrites (Hynes et al., 2003; Mandt et al., 2008; Scott & Tanaka, 1982; Tanaka, 2000). Study region one is located within a collapse feature just north of the Apollinaris Mons caldera. Collapse features are typically interpreted as the result of subsurface collapse or movement and are commonly associated with the release of volatiles (Mandt et al., 2008; McColley et al., 2005). This area was chosen because it retains surface temperatures above the atmospheric temperature for the entire ROTO observational period, which allowed for a complete surface emissivity analysis at each ROTO emission angle (Figure 3).

Study area 2 is located at the southwestern edge of the Apollinaris Mons fan deposit before it meets chaos terrain. This unit falls within the fan deposit south of the Apollinaris Mons caldera, which has previously been described as rolling plains composed of volcanic material overlain by aeolian deposits (Chuang et al., 2019; Scott et al., 1993). After emanating from a ~2 km wide channel in the caldera rim, the fan deposit covers much of Apollinaris Mons' south flank with a runout distance of ~150 km. Bisecting the fan are numerous channels interpreted as pyroclastic flows, lahars, or other fluvial processes (El Maarry et al., 2012; Farrell & Lang, 2010; Gregg & Krysak, 2011; Gulick & Baker, 1990). Impact craters in the fan deposit display a layered texture on their walls, with some exhibiting rampart ejecta indicating a volatile-rich substrate at the time of impact (El Maarry et al., 2012; Lang et al., 2010).

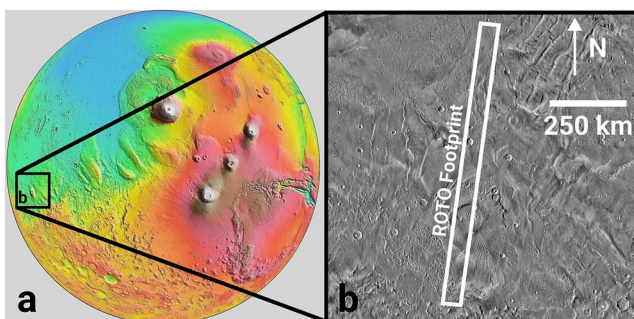


**Figure 1.** (a) Mars Orbital Laser Altimeter topographic map showing the location of the study region near Apollinaris Mons. (b) Thermal Emission Imaging System daytime image mosaic with the March 2021 a Routine Off-nadir Targeted Observations footprint shown.

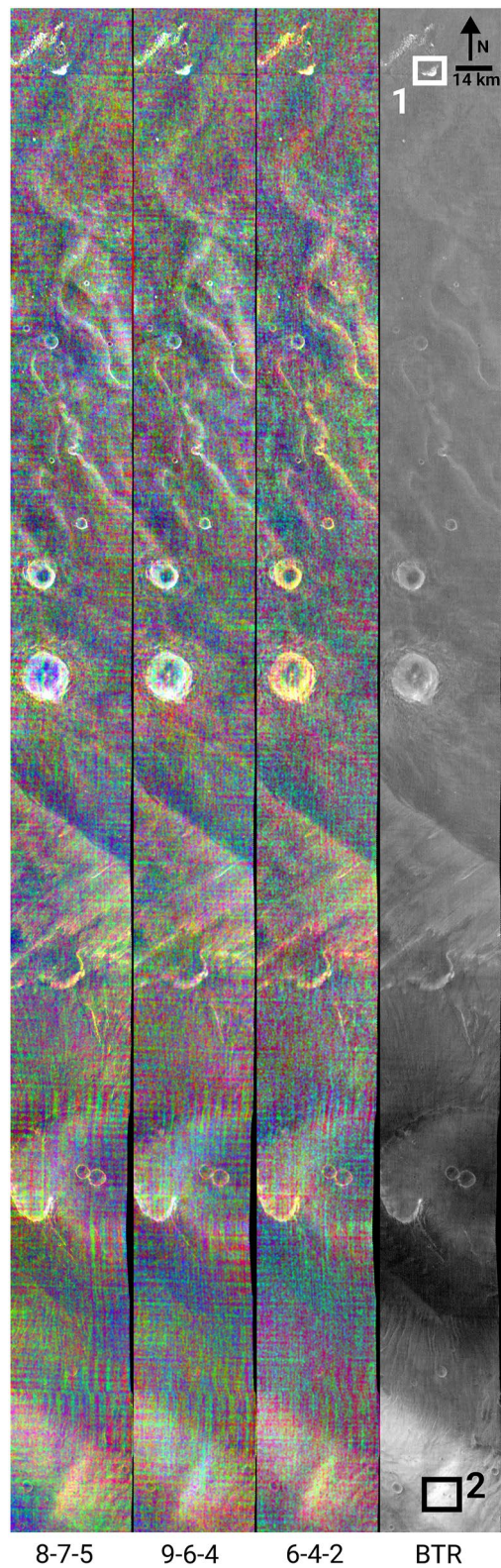


**Figure 2.** Thermal Emission Imaging System (THEMIS) 4-panel plot of the Routine Off-nadir Targeted Observation data (ID# I86177001) centered near 174°E, 8°S. The three left images are decorrelation stretch images of THEMIS radiance using bands 8-7-5, 9-6-4, and 6-4-2, respectively. The fourth image is the derived brightness temperature. Study areas 1 and 2 are shown in the white and black boxes.

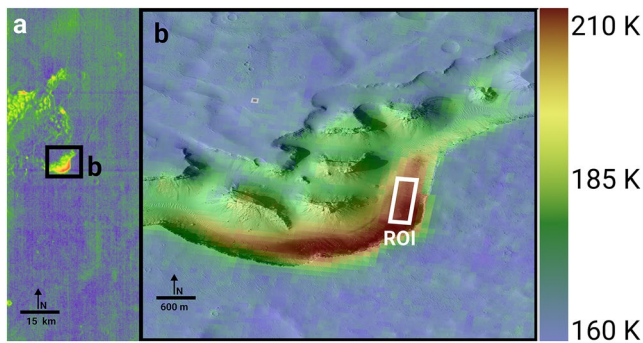


**Figure 3.** (a) Colorized brightness temperature (BT) image showing study area 1. Warmer colors indicate higher temperatures. (b) Colorized BT image overlain on High Resolution Imaging Science Experiment image ESP\_047230\_178. The white box indicates the region of interest used for spectral emissivity extraction.

Due to the season, overpass time, and TI, much of this surface has BT values below 200 K. These temperatures generally fall below the atmospheric temperature at this time of day and require the use of BT analysis instead of emissivity. Area 2 lacks the large-scale topographic slopes observed in study area 1 but displays warmer BT than the surrounding terrain (Figure 4).

### 3.2. THEMIS Instrument and ROTO Data Description

THEMIS uses an uncooled microbolometer array with nine spectral channels between 6.8 and 14.9  $\mu\text{m}$ . The instrument acquires TIR data at a spatial resolution of  $\sim 100$  m/pixel and bandwidth of  $\sim 1$   $\mu\text{m}$  (Christensen et al., 2004). Christensen et al. (2004) and Bandfield et al. (2004) describe the radiometric calibration and associated uncertainties for the THEMIS instrument. A standard THEMIS “4-panel” decorrelation stretch (DCS) image (e.g., Gillespie et al., 1986) set was used to identify regions where dominant spectral slopes are present (Bandfield, 2009; Osterloo et al., 2008). DCS images use THEMIS calibrated spectral radiance displayed in three different band ratios and a corresponding surface temperature image (e.g.,

Bandfield, 2006, 2008, 2009). This process removes highly correlated spectral data, enhancing the color differences between spectral channels. Here, pixels with anisothermal spectra appear as blue or cyan pixels indicating a negative spectral slope (Figure 2).

Where possible, atmospherically corrected surface emissivity spectra were obtained using the methods described in Bandfield et al. (2004). This technique assumes an invariant atmosphere over the study area. It provides a straightforward approach to removing atmospheric emission and scattering by first choosing a region of variable temperature but uniform composition within the THEMIS scene. A Surface emission spectrum obtained from

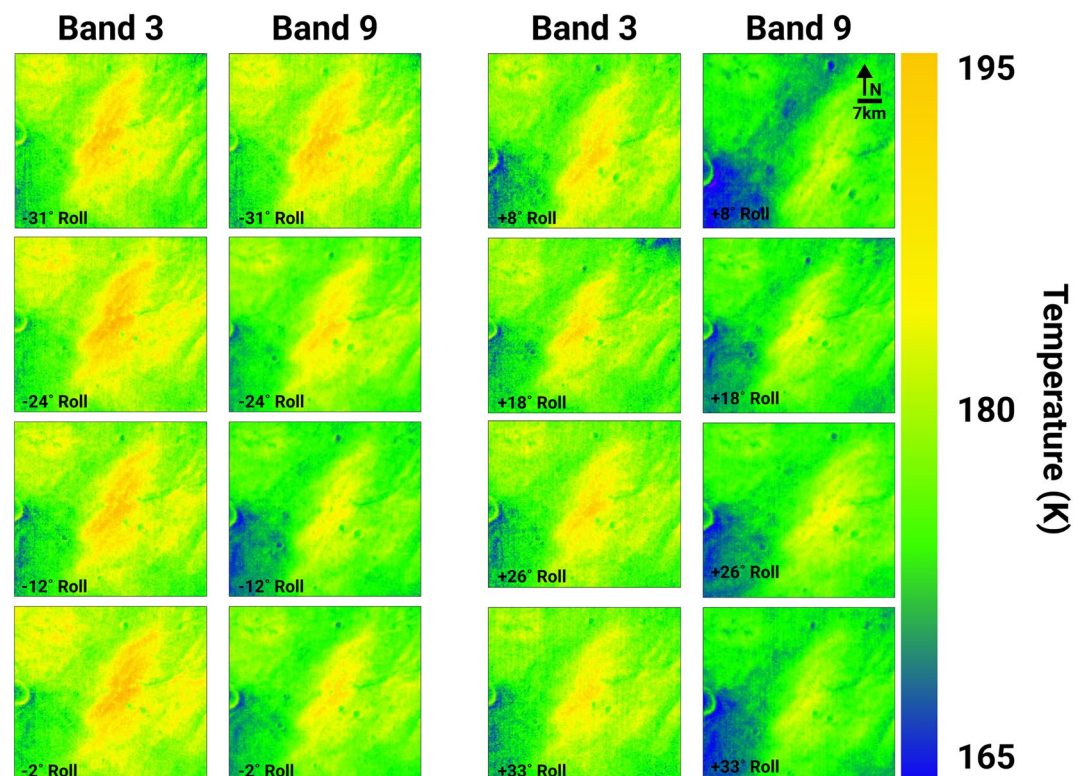


**Figure 4.** Band 3 and 9 colorized brightness temperature (BT) images at Study Area 2 demonstrating the change in observed BT as a function of emission angle.

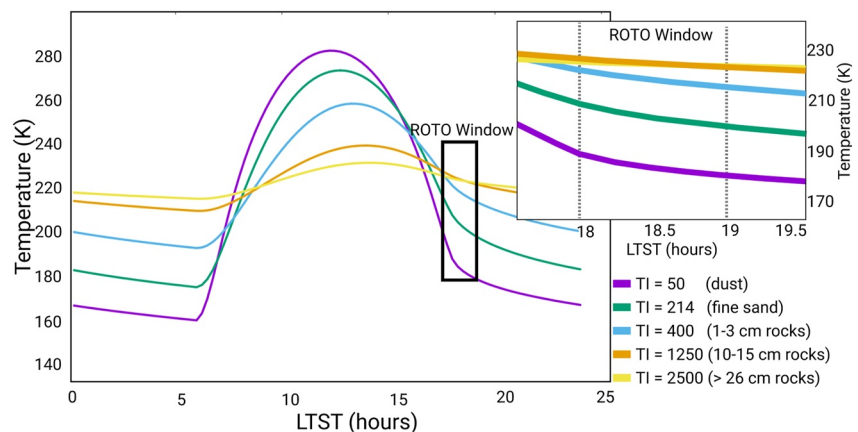


**Figure 5.** Diurnal curve of different materials with thermal inertia (TI) values ranging from 50 to 2,500 thermal inertia units (TIU). Surface units with TI values above 1,250 TIU produce temperatures indistinguishable from one another and are inseparable in the thermal model.

Mars Global Surveyor Thermal Emission Spectrometer (TES) data is used to calculate and remove the atmospheric spectral signal. The TES-derived atmospheric properties are then removed from the THEMIS data on a pixel-by-pixel basis, resulting in atmospherically corrected THEMIS surface emissivity data (Bandfield, 2008; Bandfield & Smith, 2003; Bandfield et al., 2004; M. D. Smith et al., 2000). This approach is only valid where surface temperatures exceed atmospheric temperatures.

Since 2014, the Mars Odyssey spacecraft has followed the terminator, allowing for dusk and dawn observations. Although this provides unique viewing conditions and high solar illumination angles that accentuate topographic features, it has created thermal challenges where attempting to quantify the surface contribution to the measured radiance. In cases where the atmospheric temperature exceeds the surface temperature, atmospheric emission dominates the radiance spectrum and effectively masks surface emission over much of the THEMIS wavelength region. Under these atmospheric conditions, temperature differences on the surface can be inferred by examining the BT differences between wavelengths where atmospheric emission is minimal. This study uses derived BT differences between THEMIS bands 3 and 9 collected from opposing ROTO emission angles.

Brightness temperature is calculated by fitting a Planck curve to channels 3 (7.93  $\mu\text{m}$ ) and 9 (12.57  $\mu\text{m}$ ). Wavelength-dependent brightness temperatures are then averaged over each region of interest (ROI). Band 3 is chosen as the atmosphere is relatively transparent at this wavelength, and the surface emissivity of most rock-forming minerals is near unity. However, band 3 can be noticeably impacted by dust and water ice in the atmosphere (M. D. Smith et al., 2003). Band 9 was chosen as it contains the highest signal to noise and is also relatively transparent to atmospheric dust, although the wings of the atmospheric  $\text{CO}_2$  absorption band may be detected at colder surface temperatures. To accurately predict the effects of sub-pixel heterogeneity on the measured BT or emissivity, a model forecasting both realistic temperatures is required (Bandfield, 2009; Bandfield & Edwards, 2008).

### 3.3. Modeling Approach

This study utilizes wavelength and viewing angle-dependent differences in emissivity or BT to separate thermally mixed surface units. To achieve this, we forward model the TIR spectral slopes or band-dependent differences in BT using a two-component thermal model. Here, we consider rocks as blocks 10 cm or greater. This approximation is based on the sensitivity of the TIR spectrum and the separability of the diurnal curves for materials with distinct TI values (Figure 5). At the LTST of the ROTO collection, surface units with TI values up to 1,250 TIU are distinguishable from one another, whereas TI values from 1,250 to 2,500 TIU produced inseparable surface temperatures. On Mars, TI values of 1,250 represent particle sizes of 10–15 cm, and TI values of 2,500 represent blocks >26 cm (Figure 5) (Bandfield & Edwards, 2008; Ferguson et al., 2006; Nowicki & Christensen, 2007; Presley & Christensen, 1997).

Using the KRC model (V 3.5.6, Kieffer, 2013), we predict surface temperatures for a range of TI components at each THEMIS ROTO observation used in this study. Model inputs account for latitude, longitude, local time, and solar longitude ( $L_s$ ), albedo, elevation, slope, dust albedo, and visible dust opacity at the observation time. Albedo input values are obtained from a 2 pixel per degree (ppd) TES global albedo map, and dust opacity was extracted from the dust climatology database (Montabone et al., 2020) using the latitude, longitude,  $L_s$ , and Mars year. The KRC model is capable of successfully modeling complex surface types and thermophysical properties (e.g., Ahern et al., 2021; Armstrong et al., 2005; Bandfield & Edwards, 2008; Bandfield & Feldman, 2008; Edwards et al., 2009; Fergason et al., 2006; Kieffer et al., 2006; Titus et al., 2003). KRC assumes a one-layer atmosphere coupled to the surface by solar (spectrally gray) and thermal radiation (isotropic and spectrally gray) and predicts surface temperatures by solving the heat conduction equation through forward-finite differences. The model accounts for condensation and atmospheric pressure variation, down-welling radiation, upwelling radiation, direct and diffuse insolation, an insulating primary layer, and the latent heat of  $\text{CO}_2$ , if saturation temperature is reached (Ahern et al., 2021; Kieffer, 2013).

Using the predicted temperatures from KRC, sets of simulated blackbody spectral radiance is calculated for each TI component. Radiance spectra are given “spectral color” by multiplying the radiance values by the TES high albedo surface emission spectra obtained from the Arizona State University (ASU) Spectral Library and down-sampled to the THEMIS band filters (Christensen et al., 2000).

Assuming that the measured surface emissivity is a combination of surface dust, rock, and sand, radiance spectra are mathematically mixed in combinations of two endmember abundances (90/10, 80/20, 70/30, etc.) to produce a new mixed temperature simulated radiance spectrum. This method is effective as radiance curves of spatial mixtures mix in a linear fashion (Audouard et al., 2014; Bandfield, 2009; Nowicki & Christensen, 2007; Ramsey & Christensen, 1998). Finally, emission spectral slopes are simulated by dividing the mixed temperature radiance spectrum by the Planck radiance at THEMIS band 3 (7.93  $\mu\text{m}$ ). This method of emissivity separation is identical to the one applied to THEMIS measured radiance, allowing for a direct comparison (Bandfield, 2009).

If surface temperatures are too cold to allow for accurate emissivity retrieval, BT is calculated at bands 3 (7.93  $\mu\text{m}$ ) and 9 (12.57  $\mu\text{m}$ ). THEMIS BT measured at band 9 is compared to the modeled BT calculated from the KRC-derived spectral radiance. As band 9 is the most atmospherically transparent, it is considered the closest to the kinetic surface temperature. Here, we use the BT difference between bands 3 and 9 as a proxy for spectral slopes in emission data and an indicator of sub-pixel temperature mixing. Apparent and simulated brightness temperatures are calculated using a look-up table of calculated bolometric Planck radiances. In short, the look-up tables consist of the THEMIS filter functions convolved with the Planck curve (assuming an emissivity of unity). Measured radiance is passed through the look-up table to determine what temperature produces the measured radiance in each band. The highest BT is assumed to equal the true surface kinetic temperature. The function repeats to determine the emissivity and BT in the other THEMIS bands (Christensen et al., 2004). Ultimately, surface emissivity modeling and BT modeling provide a means to estimate the sub-pixel surface unit abundance. Modeled surface unit abundance derived from spectral emissivity modeling is the preferred approach as it employs the entire THEMIS spectral range and provides greater leverage of the complete data compared to the BT approach.

### 3.3.1. Rock Abundance Modeling

Significant relative proportions of visible (and less dust-covered) rock increase the magnitude of the observed emissivity spectral slopes. In other words, a more considerable ratio of a high TI, rocky surface surrounded by low TI dust produces emission spectra with a steeper spectral slope toward longer wavelengths. To evaluate the effects of anisothermality caused by differences in TI of the surface units, synthetic emission spectra, and brightness temperatures are modeled at each of the observed ROTO viewing geometries. For colder surfaces, the available wavelength possibilities due to atmospheric emission are limited (e.g., area 2), and the simpler two-band BT model is employed.

Because an object's TI depends on its thermal conductivity, particle size can be inferred from an object's TI value. Lower TI values indicate fine particle size materials, whereas higher TI values indicate larger particle sizes (Ahern et al., 2021; Dollfus & Deschamps, 1986; Fenton et al., 2003; Jakosky, 1986; Nowicki & Christensen, 2007; Piqueux & Christensen, 2011; Ruff & Christensen, 2002). At the sub-pixel scale, surface unit discrimination depends on the temperature contrast between those surface units (Coward & Rogers, 2021). Over the LTST of the

**Table 2**  
*Model Uncertainties and Associated Errors*

Precision	Modeled sensitivity	Percentage temperature change
Brightness temperature	1.2 K	6%
Albedo	0.05	0.5%
Dust opacity	0.09	0.5%–1%
Pixel elongation	1 px	16%
Detector timing	1–2 px	8%
Pointing position	1 px	16%
<b>RSS</b>		<b>15.6%</b>

*Note.* Percent errors are combined using a root square sum (RSS) method as model parameters are uncorrelated.

eight ROTO overpasses (18–19 hr), the KRC (Kieffer, 2013) thermal model was used to predict the temperatures for surface units with TI values correlating to Martian dust (50 TIU), sand (214 TIU), duricrust (600 TIU), and rocks of 0.1–0.15 m (1,250 TIU) with the estimated TI values for each component taken from Presley and Christensen (1997) and Golombek et al. (2003).

### 3.4. Sensitivities and Uncertainties

Aspects of the TIR measurement and models described here have associated uncertainties and sensitivities. These are presented in Table 2 and described in detail below. Sources of uncertainties in the model include (a) uncertainties in THEMIS brightness temperatures, (b) model sensitivities due to uncertainty associated with the values of various surface and atmospheric parameters (albedo, dust column opacity, etc.), and (c) uncertainties in ROTO viewing geometry (pixel elongation, detection timing, and pointing position) (Table 2).

#### 3.4.1. Surface Temperature Derivation

THEMIS BT is determined by comparing the scene's radiance with the internal reference calibration flag measured in eight-bit data numbers. This method can produce several factors that complicate THEMIS data calibration and BT derivation, the most dominant of which is atmospheric gas and aerosol absorptions. Typically, this can result in a 10–15 K underestimation of surface temperatures if viewing a warm surface through a cold atmosphere (Bandfield & Edwards, 2008). We attempt to minimize atmospheric effects by completing a full atmospheric correction of the data. Additionally, the near symmetry of the ROTO produces observations with similar atmospheric path lengths, further diminishing potential atmospheric effects between paired observations (–31 and +33, –24 and +26, etc.).

The absolute calibration of THEMIS nighttime images also produces uncertainties associated with the instrument's internal calibration. Ferguson et al. (2006) and Bandfield et al. (2004) offer a thorough discussion of these. To summarize, the uncertainty analysis reported in Ferguson et al. (2006) concluded that brightness temperatures are calibrated to a precision of 1.2 K and absolute accuracy of 2.8 K at night (Ferguson et al., 2006).

#### 3.4.2. Model Sensitivities Due To Uncertainties Associated With Surface Parameters

To test the sensitivity of the two-component TI model, we chose to investigate the effects of incorrect TI, albedo, and atmospheric dust opacity on the model results. We used TI values between 50–100 TIU in 10 TIU increments and between 800–2,500 in 100 TIU increments to simulate dust and rock of different particle sizes (Presley & Christensen, 1997). The change in TI from 50–100 TIU results in an  $11 \pm 2$  K variation in predicted surface temperature for the fine particle size component. This represents BT values of 182–193 K. Varying the TI of the rock component results in a  $6 \pm 3$  K variation in predicted surface temperature from 217 to 223 K. These new values for high and low TI components are used to assess the associated uncertainties and sensitivity of the two-component mixing model. We calculated model fits using an unconstrained linear least squares fitting analysis to determine the root mean square (RMS) error and median absolute deviation (MAD). As the measured spectra fall within  $\sim 0.9$ –1 emissivity, we define significance in the model as RMS error values  $\leq 0.03$  or  $3\sigma$  of the standard deviation in RMS error.

At site 1, an increase of 11 K for the dust component does not produce a significant model fit to the measured spectra and results in an RMS error of 0.07 and MAD of 0.05 between the measured and modeled spectra (Figure 6). Variation in the high TI component from 217 to 223 K results in a minimal

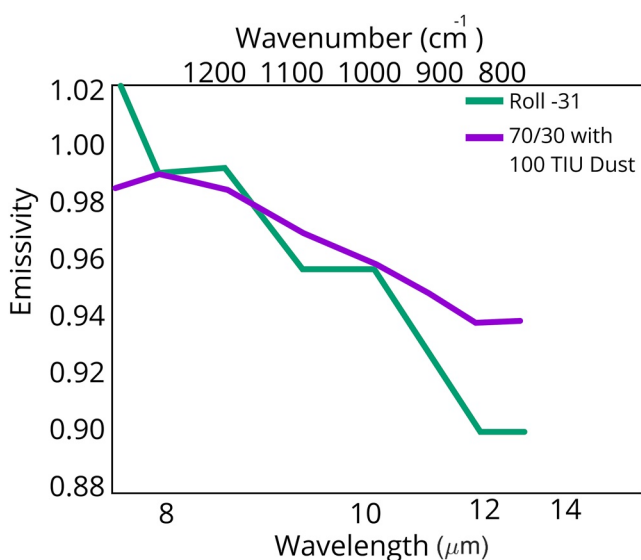


**Figure 6.** Spectral slope sensitivity analysis using 100 thermal inertia units (TIU) dust in a 70/30 mixture, changing the thermal inertia values for dust from 50 to 100 TIU results in a non-significant spectral slope match.

**Table 3**  
*Measured Brightness Temperature Results-Study Site 2*

Image ID	Roll (°)	B3 temp (K)	B9 temp (K)	Difference (B3 – B9) (K)	Time (hr)	$L_s$ (°)	Emission angle (°)	Incidence angle (°)
I86177001	–31	193.8	191.6	2.2	18.2	47.0	35.3	95.0
I86202001	–24	194.5	191.9	2.6	18.3	47.9	27.2	96.0
I85939006	–12	193.7	190.2	3.5	18.3	38.3	13.4	95.5
I85964009	–2	194.7	191.6	3.1	18.4	39.2	2.6	96.9
I85989005	+8	192.9	187.9	5	18.5	40.2	10.2	98.0
I86014012	+18	192.4	189.8	2.6	18.6	41.1	20.3	99.6
I86039007	+26	192.2	189.4	2.8	18.6	42.0	29.4	100.8
I86064009	+33	192.4	188.5	3.9	18.7	42.9	37.5	102.1

variance from the modeled results, increasing the modeled RMS error from 0.03 to 0.05. The derived RMS error represents a  $\pm 5\%$  distribution of components for each model run. The nadir viewing geometry at study region 1 is an exception, and the associated error is  $\pm 3\%$  of the modeled component ratio.

Where relying solely on BT differences, variations in the modeled BT and TI result from small changes in the component ratios in the model. For example, at study site 2, the best model fit was produced using a dust-to-duricrust ratio of 75/25 instead of dust-to-rock, as used in site 1. This mixture resulted in the closest fit to the measured BT and derived TI (Table 3). However, varying the dust/duricrust ratio by  $\pm 5\%$  results in a modeled TI for the mixture that differs from the THEMIS-derived values by  $\pm 27$  TIU and a modeled BT at band 9 that varied from measured values by  $\pm 5$  K (Table 4). Although the difference in BT between bands 3 and 9 remains relatively low at 3–5 K. This indicates that although effective, rock abundance modeling based on differences in BT does not provide the same precision in percent cover estimation as spectral slope modeling.

### 3.4.3. Uncertainties Associated With Albedo and Atmospheric Properties

Albedo and atmospheric dust opacity play a less drastic role in predicting surface temperature with KRC. We obtained surface albedo values from the THEMIS VIS-ALB images for the study region. As the ROTO images are collected just after sunset, uncertainty in albedo is relatively high as less time has passed for the daytime albedo effects to diminish. Using KRC, we tested an albedo uncertainty of 0.05, which resulted in a predicted surface temperature of  $\pm 2$  K. Overall, this had little to no impact on the simulated emissivity spectral slopes. The associated RMS errors between measured and modeled spectra varied by  $< 0.002$ .

Atmospheric dust opacity (TAUD) was obtained from Montabone et al. (2020). TAUD values are obtained from the same  $L_s$  and geographic location as the THEMIS temperature data. As this data is a new ROTO data set collected in Mars Year 36, the Mars Climate Database does not yet contain atmospheric dust opacity values during these observations. Instead, we used values for Mars year 34. Due to the lack of THEMIS data, IR values are multiplied by 2.6 as recommended by Montabone et al. (2020). Associated uncertainty with atmospheric dust opacity is an average of 0.09 for Mars Year 34 over the  $L_s$  of ROTO acquisitions, which are adopted here.

### 3.4.4. Uncertainties in ROTO Viewing Geometry

Due to the ROTO's unique pointing capabilities, uncertainties in the surface footprint size represent the largest source of uncertainty in these observations and the model results. To compare surface characteristics at different emission angles, the pixels used in each observation must be statistically similar in surface units, distribution, and physical properties. Changes in albedo, TI, and areal distribution of surface units between the ROTO measurements are

**Table 4**  
*Model Results From Study Region 2 Showing the Simulated Brightness Temperature (BT) and Thermal Inertia (TI) for Model Runs Compared With the Measured BT Averaged Across Bands 3–9 and Derived Thermal Emission Imaging System TI for the Study Region*

Mixture ratio	Bands 3–9 simulated BT (K)	Simulated TI (TIU)
Measured results	193–190 $\pm$ 2.8 K	185 $\pm$ 12
80/20 dust/duricrust	188–185 $\pm$ 3	160 $\pm$ 6
75/25 dust/duricrust	190–187 $\pm$ 3	187 $\pm$ 6
70/30 dust/duricrust	198–192 $\pm$ 3	215 $\pm$ 6
70/30 dust/rock	215–205 $\pm$ 3	410 $\pm$ 6
75/25 dust/rock	212–207 $\pm$ 3	350 $\pm$ 6
80/20 dust/rock	210–205 $\pm$ 3	290 $\pm$ 6

due to errors in instrument pointing and will have a significant effect on the derived model abundances. Additionally, due to the off-nadir viewing geometry, pixel areas can become elongated, covering more of the surface instead of their typical 100 m in nadir data.

We divide errors in surface footprint into two main categories, those related to uncertainty in the timing of the detector and those related to accuracies in spacecraft pointing/orbital position. Errors in detector timing only occur in the along-track direction and result in  $\pm 1$ – $2$  pixels of uncertainty which follow a Gaussian distribution. This indicates that most errors are on the sub-pixel to one-pixel level. Inaccuracies in the spacecraft pointing/orbital position result in  $\pm 1$  pixel error and occur in both the along-track and cross-track directions. We utilize averaged TIR emission spectra and BT over multiple pixels in the ROIs to reduce the uncertainty in the THEMIS measurement. Pixel elongation introduces the largest source of error and is most dominant at the larger rolls of  $-31$ ,  $-24$ ,  $+26$ , and  $+33$ . Here we estimate that pixel elongation accounts for  $\sim 1$  pixel worth of error or  $\sim 16\%$ .

### 3.5. TIR Sensitivity and Scale of Surface Features

TIR data are sensitive to the scale at which the facets of surface units remain thermally isolated. We estimate the spatial sensitivity based on the surface's TI. At low TI ( $<100$  TIU), the TIR spectrum is sensitive to features on a scale of  $\sim 1$  cm. At a moderate TI ( $150$ – $300$  TIU), the scale of sensitivity increases to  $\sim 10$  cm, and at high TI ( $>800$  TIU), the scale is  $\sim 1$  m (Bandfield & Edwards, 2008). Nighttime thermal emission measurements, on the other hand, provide qualitative information on relative differences in surface particle size, degrees of inundation, and total rock abundance (Ahern et al., 2021; Christensen, 1986; Fergason et al., 2006; Kieffer et al., 1977). After sunset, with solar forcing removed, surface units thermally equilibrate at a rate directly proportional to their TI, if thermal diffusion allows anisothermality to exist in the first place. The surfaces studied here have THEMIS-derived TI values between  $150$  and  $350 \text{ J m}^{-2} \text{ K}^{-1} \text{ s}^{-1/2}$  (Fergason et al., 2006). This constrains the TIR sensitivity to temperature mixing at the  $\sim 10$  cm scale, five times smaller than High Resolution Imaging Science Experiment (HiRISE) spatial sampling ( $54.4 \text{ cm/pixel}$ ) and a scale previously only accessible by in-situ investigation.

## 4. Results

### 4.1. Brightness Temperature Results

All images used in this study are collected at LTST between 18:00–19:00 hr with emission angles between  $2^\circ$  and  $37^\circ$ . However, due to the off-nadir geometry of the ROTO acquisitions, the effective phase angle between the solar incidence and emission angles ranges from  $59^\circ$  to  $139^\circ$ . In study area 1, the eight post-sunset observations have temperature asymmetries about the  $-2^\circ$  roll angle (effectively nadir), with the lowest temperatures recorded at the highest emission angles ( $33^\circ$  and  $-31^\circ$ ). Negative roll angles favor western-facing slopes and show higher overall temperatures than positive roll angles of a similar magnitude. This corresponds to slopes recently illuminated by the western setting sun. Study region 2 has lower average surface brightness temperatures than area 1. A maximum BT of 191 K at the  $-31^\circ$  ROTO roll and a low of 187 K at the  $+8^\circ$  ROTO roll is observed (Figure 4, Table 3). The ROTO roll angle of  $+8^\circ$  shows the greatest temperature difference between THEMIS bands 3 and 9 at  $\sim 5$  K, and the smallest difference is observed in the  $-31^\circ$  ROTO at  $\sim 2$  K. At study site 2, differences in BT between spectral channels decrease as the viewing angle moves to the more extreme positive and negative roll angles, indicating a decrease in anisothermality at higher emission angles. The opposite as observed in study area 1.

### 4.2. Surface Emissivity Results

A six-pixel ROI within study area 1 was chosen where the surface temperatures remained well above the atmospheric temperatures in all the THEMIS ROTO images. A consistent negative spectral slope is apparent in the extracted emission spectra from the ROI. Generally, ROTOs with a negative roll angle ( $-31^\circ$ ,  $-24^\circ$ , and  $-12^\circ$ ) show negative spectral slopes of a greater magnitude than those extracted from ROTOs with positive roll angles ( $+33^\circ$ ,  $+26^\circ$ ,  $+18^\circ$ , and  $+8^\circ$ ), the exception to this is the  $-2^\circ$  (e.g., nadir) which displays the lowest magnitude spectral slope. Where comparing emission spectra from complementary ROTO angles (e.g.,  $-31^\circ$  and  $+33^\circ$ ,  $-24^\circ$  and  $+26^\circ$ , etc.), the endmember pairs ( $-31^\circ$  and  $+33^\circ$ ) show the largest difference in spectral slopes, whereas intermediate pairs ( $-12^\circ$  and  $+18^\circ$ ,  $-24^\circ$  and  $+26^\circ$ ) show less of a difference (Figure 7). Where plotted

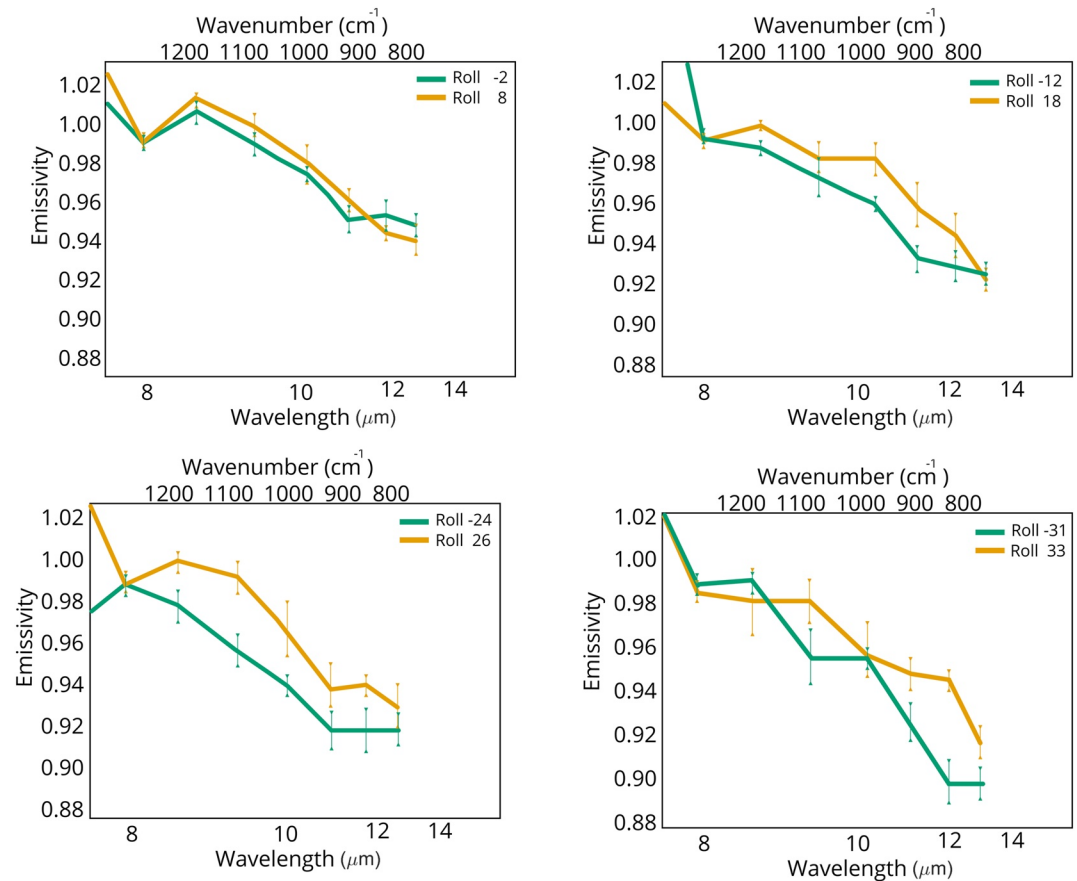


**Figure 7.** Thermal Emission Imaging System emission spectra from each paired Routine Off-nadir Targeted Observation observation averaged over the study region of interest (ROI) in Figure 3. Endmember roll angles ( $-31^\circ$  and  $+33^\circ$ ,  $-2^\circ$  and  $+8^\circ$ ) show the largest difference in spectral slope, whereas intermediate roll angles ( $-12^\circ$  and  $+18^\circ$ ,  $-24^\circ$  and  $+26^\circ$ ) show the smallest difference. Error bars represent the ROI's maxima and minima of band dependent emissivity.

together, the measured emissivity spectra may constitute a continuum of spectral slopes beginning at the  $-2^\circ$  roll and ending at the  $-31^\circ$  roll. As the spectral slope is directly correlated to the magnitude of sub-pixel temperature mixing within the instrument FOV, this observed range in slopes provides valuable insight into surface conditions at each viewing geometry. Furthermore, it demonstrates that ROTO observations provide a comprehensive view of surface features below the instrument's spatial resolution that would typically require repeat nadir observations over long timescales.

### 4.3. Rock Abundance Modeling

Using the methods outlined in Section 3.3.1, we analyzed the effects of sub-pixel anisothermality by forward-modeling the emissivity spectral slopes for a range of two-component surfaces (i.e., rock and sand, rock, and dust). The relative proportion of distinctly different surface units is apparent by varying the emission angle. For example, off-nadir emission angles are more effective at viewing the sides of warm rocks mantled or capped by dust. Here, we define “rocks” as objects 10 cm or larger with a TI of 1,250 TIU or greater.

Where surface units exhibit significant temperature differences, an increase in the spectral slope magnitude is observed (i.e., cold dusty surfaces and warm rocks). Sand and dust contributions were varied from 60% to  $95\% \pm 5\%$  relative to the respective rock and regolith components. The resulting mixed TI radiance spectra are converted to emissivity resulting in sloped emission spectra similar to the observed ROTO emission spectra. Using the resulting synthetic spectra, we create a rock abundance model to represent the distribution of different surface units observed at each viewing geometry.

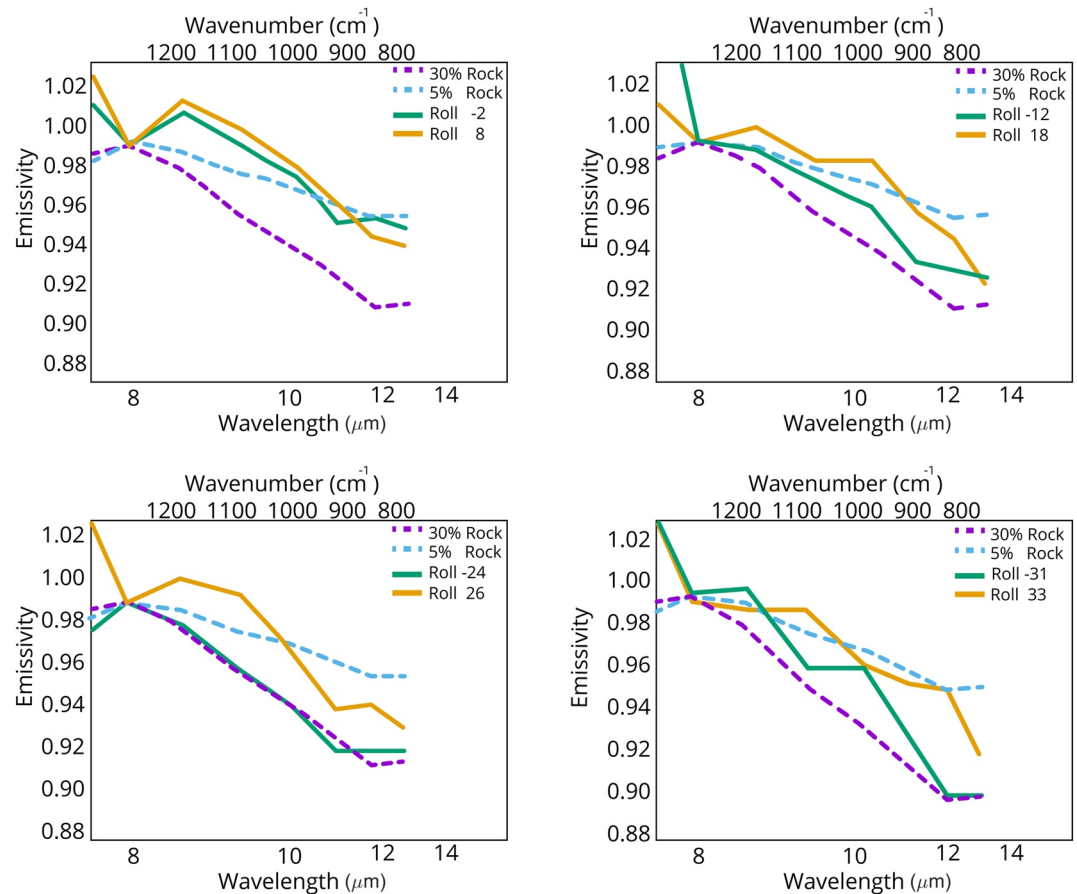


**Figure 8.** Simulated surface emissivity spectra modeled using the viewing parameters from Study Area 1 listed in Table 1. Spectra for eight different viewing geometries are shown. An averaged Martian high albedo surface spectrum was convolved with the modeled blackbody spectrum to add “spectral color.” The negative spectral slopes are due to differences in temperature caused by varying distributions of surface units with differing thermal physical properties at each viewing geometry.

For site 1, model combinations containing varying percentages of rock (1,250 TIU) and dust (50 TIU) produced mixtures that best match the surface's observed bulk TI and temperature. The simulated anisothermal emission spectra for study area 1 are shown in Figure 8. Emission spectral slope modeling indicates that the higher magnitude off-nadir rolls best match the higher rock abundance models. A rock abundance upwards of  $30 \pm 5\%$  best matches the higher magnitude emission angles with an RMS error of 0.03 and a MAD error of 0.02. As rolls approach nadir, the observed spectral slope decreases and more closely matches the lower rock abundance model of  $5 \pm 3\%$  with an RMS error of 0.04 and a MAD error of 0.03. This supports our hypothesis that higher off-nadir emission angles are more effective at viewing the warm sides of dust capped rocks. Additionally, it suggests that traditional methods utilizing nadir observations to derive rock abundance only account for the presence of 1/6 of the predicted total rock abundance, resulting in a drastic underestimation.

As the modeled percentage of rock and dust increases, the modeled spectral slope increases. Our modeling predicts that this trend will continue until a maximum temperature difference is reached. Under the ROTO observing conditions, this occurs around 40% rock and 60% dust  $\pm 5\%$ . At this point, the trend reverses, and the modeled spectral slope decreases. At higher rock percentages, the warm rock surfaces dominate the TIR radiance, and the temperature difference between warm and cold surfaces decreases. Additionally, the 40/60  $\pm 5\%$  distribution of dust and rock has a nearly identical spectral slope to that of a surface with 90/10 dust and rock  $\pm 5\%$  (Figure 9). However, the modeled apparent BT and model integrated TI vary for these two surfaces allowing for identification between the two distributions of surface units.

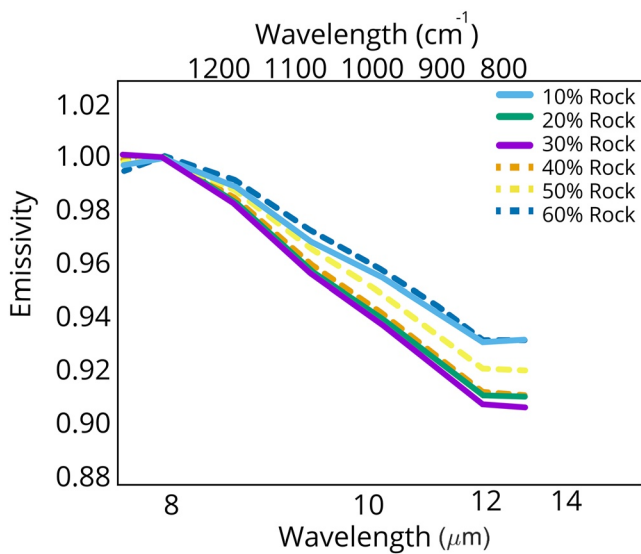


**Figure 9.** Synthetic emission slopes are created for varying mixtures of rock and dust. Adding a more significant percentage of rock into the mixture increases the spectral slope until a 30/70 rock to dust ratio is reached. After this point, the trend reverses, and spectra become less sloped.

Due to the cold surface temperatures ( $<200$  K), rock abundance is derived at study area 2 using BT modeling. Results indicate a mixture of low TI (50 TIU) dust and a duricrust-like surface (600 TIU) in a 75/25 ratio. This mixture produces a model-integrated (weighted average) TI of  $187 \pm 6$  TIU, close to the previous THEMIS-derived bulk TI for this region ( $185 \pm 12$   $\text{J m}^{-2} \text{K}^{-1} \text{s}^{-1/2}$ ) from Ferguson (2014). The modeled BT range of 190–187 across bands 3–9 closely matches the average measured BT between bands 3–9 of  $193\text{--}190 \pm 2.8$  K.

## 5. Discussion

In the post-sunset observations investigated here, we proposed that the observed sub-pixel thermal heterogeneities result from mixtures of surface units with varying TI values cooling at different rates. At night, warmer temperatures represent surfaces dominated by a more significant proportion of higher TI objects (rocks), whereas cooler temperatures represent an abundance of lower TI materials (dust or sand). After sunset, lower TI materials cool quickly, and the higher TI materials retain heat longer, thus creating the observed anisothermality. Moreover, the less-dusty sides of rocks are more apparent where viewed using off-nadir observations. Dust coatings, several hundred microns in thickness, can significantly lower TI values of underlying rocky material. This effect is more drastic at dusk and nighttime, where dust quickly cools. Coatings of one diurnal skin depth ( $\sim 1$  cm) or greater can completely mask the TI signature of the underlying material (Mellon

& Putzig, 2007). Rocks capped with airfall dust may have sides that are relatively dust-free. These sides are warmed by the pre-sunset sun and thus are accentuated in the ROTO data (Figure 10). This is evident by the increased magnitude of spectral slopes observed in the off-nadir emission data and associated modeled higher rock abundance.

Temperature heterogeneities in daytime data due to surface roughness are also shown to produce negatively sloped emission spectra (e.g., Bandfield, 2009; Bandfield & Edwards, 2008; Bandfield et al., 2015). Rough surfaces undergo disproportionate solar heating and self-shadowing compared with smooth surfaces. Both surface roughness and TI differences similar affects to the TIR spectrum. However, disentangling these effects requires advanced spacecraft observations. For example, precisely timed overpasses where illumination and viewing conditions limit the impact of surface roughness and the emitted radiance is the same regardless of morphology (Davidsson et al., 2015). Lunar work under similar viewing conditions to these ROTOs demonstrates that

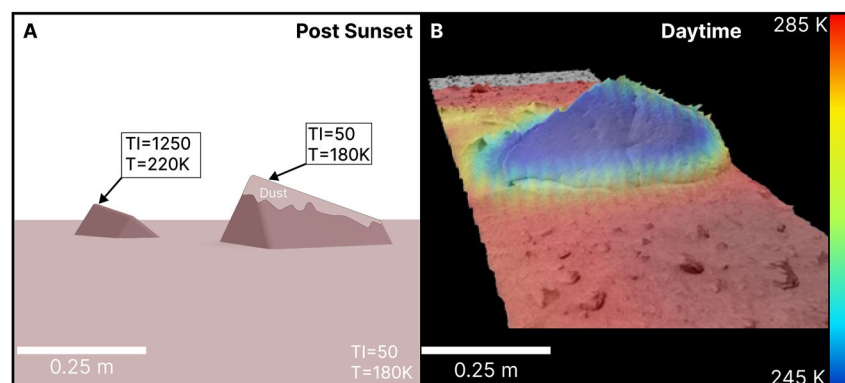


**Figure 10.** (a) Schematic illustration demonstrating the expected temperature differences between less dusty rock sides versus the dust-capped tops in post-sunset observations. (b) Colorized daytime Mini-Thermal Emission Spectrometer (TES) temperature image from the Spirit rover of the basaltic rock “Adirondack.” In daytime observations, high thermal inertias (TI) materials (rocks) appear colder than surrounding low TI materials (Mini-TES image provided by Jeff Moersch and Steve Ruff via personal communication).

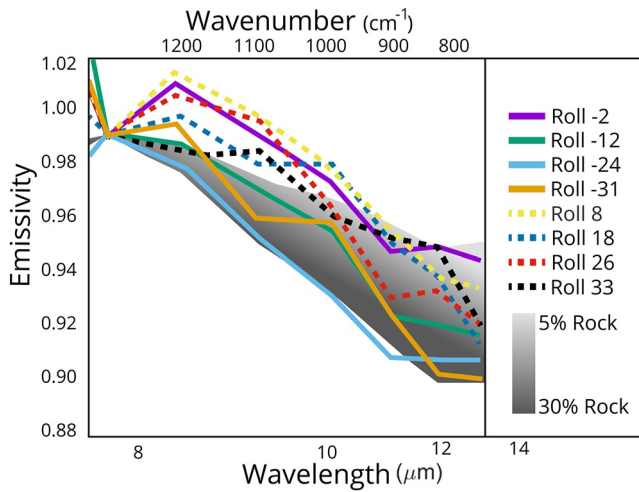


**Figure 11.** Thermal Emission Imaging System surface emissivity spectra from the collapse feature in study area 1. Negative Routine Off-nadir Targeted Observation (ROTO) angle observations are shown in solid lines, and positive ROTO angle observations are indicated as dotted lines. The shaded region denotes the range of simulated spectral slopes equating to the modeled thermal inertias (TI) mixtures. The variability in spectral slopes results from differences in the relative distribution of high and low TI units in the FOV of each observation. Positive rolls generally exhibit higher emissivity, indicating less temperature mixing and a lower modeled rock abundance.

anisothermality due to surface roughness is predominantly limited to high solar incidence angles and not significant after sunset (Bandfield et al., 2015; Rubanenko et al., 2020; Warren et al., 2019).

The work presented here concludes that surface roughness, where likely present, has minimal impact on the emitted radiance. The ROTO observations described here are conducted post-sunset, and the surface is fully shadowed. Therefore, sloped emission spectra result from temperature differences due to sub-pixel mixtures of surface units that cool at differing rates as a function of their component TIs.

### 5.1. Comparison With Previous Rock Abundance Models

The THEMIS ROTO spectral variability observed between each spacecraft overpass is consistent with that of an anisothermal surface, as described by Bandfield and Edwards (2008) and Bandfield (2009). The  $-31^\circ$  roll shows the greatest magnitude spectral slope. Spectral slopes decrease in magnitude as the emission angle decreases toward  $-2^\circ$ . Spectral slope modeling of the  $-31^\circ$  ROTO requires a higher rock abundance of 30% (Figure 11). The variability in modeled rock abundance values compared with viewing geometries indicates that higher emission angles capture a more significant proportion of high TI material than nadir viewing geometries. Prior rock abundance models describe a 3%–5% abundance of rocks with TI values above 1,250 TIU for this study region (Christensen, 1986; Nowicki & Christensen, 2007), similar to the nadir rock abundance derived here. Based on the increase in THEMIS spatial resolution and novel viewing geometry, we argue that the local rock abundance (objects > 10 cm) is likely higher, upwards of 30%, as demonstrated in the modeling of emission data collected off-nadir.

Due to the sensitivity of the TIR spectrum, materials with lower TI values (i.e., sand and duricrust) can be modeled in addition to traditional rock abundance. Brightness temperature modeling at study region 2 indicates a complex surface composed of loosely cemented material mantled by significant amounts of dust. At larger emission angles, BT differences decrease, equating to a slightly more homogeneous surface. This difference indicates more isothermal conditions at high emission angles and may suggest a greater abundance of fine-grained material or rocky material. At emission angles approaching  $0^\circ$  (Rolls  $-2^\circ$ ,  $+8^\circ$ ), the surface appears more anisothermal, indicated by the greater difference in BT between THEMIS bands 3–9 (Table 4, Figure 4). ROTO roll  $+33$  exhibits a slightly higher than expected BT difference between bands 3 and 9 and does not match the expected trend. We attribute this to roll  $+33$ 's late acquisition time at 18.7 hr.

## 5.2. Comparison to Orbital Data

### 5.2.1. Study Area 1

HiRISE image data of study area 1 shows a possible collapse feature within the lower Medusae Fossae formation (Figure 12). The ROI for this area contains the steep sides of the collapse feature rim along a north-western facing slope. Along the rim of the feature, surface material appears dark with large boulders interspersed, consistent with the modeled higher rock abundance. The floor has aeolian bedforms, indicating the presence of material transportable by the wind.

Due to the collapse feature's north-west slope orientation, ROTO observations with high magnitude negative rolls produce viewing geometries more perpendicular to the surface than those at the  $-2^\circ$  and  $+8^\circ$  observations. This higher roll angle effectively lowers the emission angle of surface units along the collapse feature slopes. Combined with the higher rock abundance near the features slope, this produces more significant checkerboard temperature mixing, resulting in the modeled higher rock abundance at negative roll angles. The THEMIS-derived TI and modeling results suggest a surface with a fine particle size component (dust-sized particles). However, dunes observed in HiRISE image data suggest sand-sized particles up to 160  $\mu\text{m}$  (Figure 12a). This discrepancy

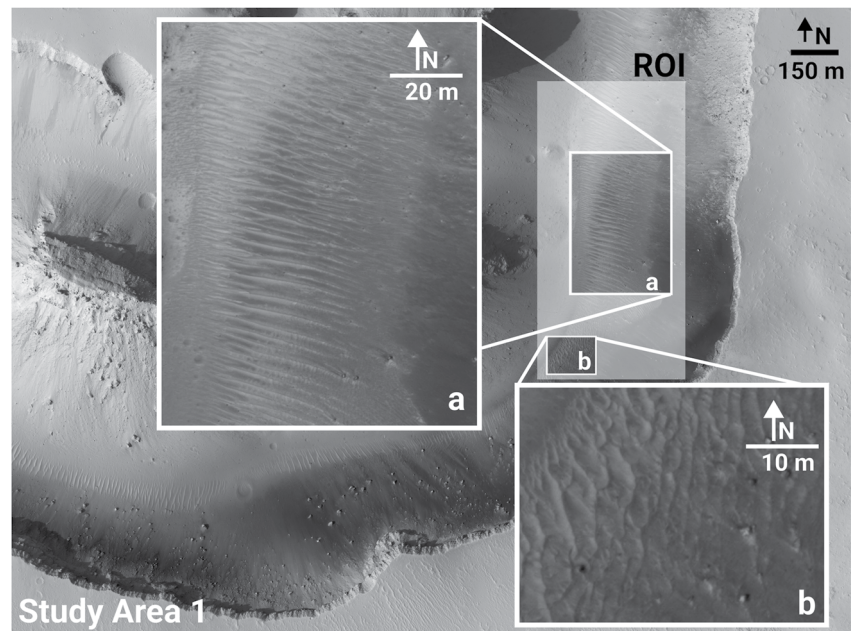


**Figure 12.** High Resolution Imaging Science Experiment image ESP\_047230\_178 of study area 1 shows the Thermal Emission Imaging System region of interest (ROI) footprint in the shaded region. Areas A and B show aeolian bedforms and larger boulders interspersed within the ROI.

may indicate the presence of vertical layering of fine materials (optically thick dust over sand) and may suggest an inactive dune environment.

Large ( $\geq 163$  cm) boulder-sized material is apparent in HiRISE images. In the TIR data, features of this size are indistinguishable from smaller cm size rocks due to the time of the Mars Odyssey overpass. Limits on temperature separability restrict the detection of rock sizes to an upper limit of 0.1–0.15 m. This represents material well below the detection limit of HiRISE image data but may be represented by the dark material along the collapse features rim and floor (Figure 12b).

### 5.2.2. Study Area 2

Mars Reconnaissance Orbiter Context Camera (CTX) image data of study area 2 reveals a complex surface dominated by impact craters and aeolian material (Figure 13). At the sub-100 m scale, the terrain appears mottled with numerous small craters. Aeolian ripples are visible on the floors of some craters and along smoother plains-like terrain. The THEMIS-derived TI values of this region are low (185 TIU), suggesting the presence of abundant fine material at particle sizes of  $\leq 100$   $\mu\text{m}$  (dust to very fine sand, Ferguson et al., 2006; Presley & Christensen, 1997). These values are consistent with the results from the TI modeling presented here, which indicates a 75/25 mixture of low TI material (50 TIU,  $\sim 1$   $\mu\text{m}$ ) and moderate TI material (600 TIU, poorly cemented material) (Table 4). Based on the endmembers used in the TI mixing model, we interpret this as an aerial mixture of volcanoclastic-like material or poorly cemented rock heavily mantled by dust.

Alternately, crater rims and ejecta blankets are shown to exhibit higher TI values than surrounding terrain (Beddingfield et al., 2018; Mellon et al., 2000). Tight groupings of small impact craters appear to behave similarly and show TI variation as a function of age and degradation (Beddingfield et al., 2021). The numerous small craters and their ejecta blankets seen in study area 2 likely represent a source of temperature variation at the THEMIS sub-pixel level. Impact gardening below the image resolution of CTX (14 m/px) may indicate the presence of a larger rock fraction and provides an alternative hypothesis for the observed anisothermality. Distinguishing between these two possibilities would require HiRISE image data for this region.

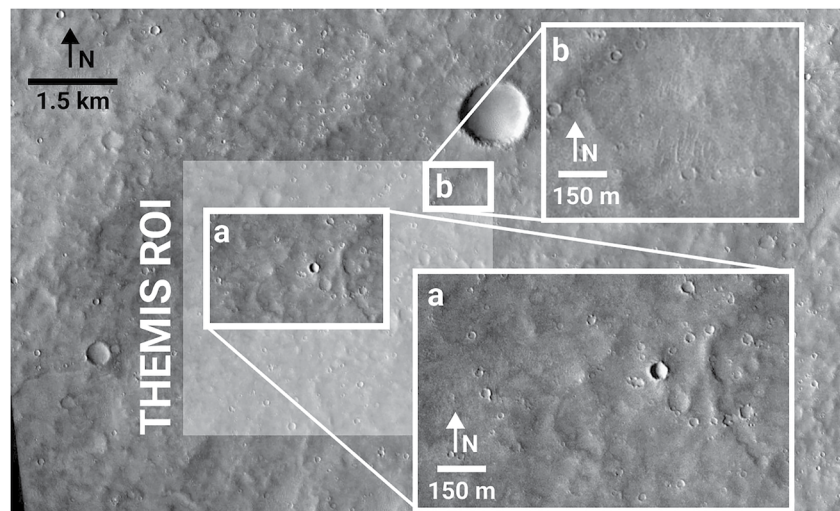


**Figure 13.** Context Camera image B05\_011653\_1714\_XN\_08S186 W of study area 2 shows abundant (a) small craters and (b) aeolian ripples.

## 6. Conclusions

Understanding the rock abundance of a planetary surface provides insight into the processes that have shaped it. Additionally, a planet's surface properties directly influence most remote sensing measurements, typically at scales well below the spatial resolution of the data. TIR spectroscopy provides a unique tool to determine sub-pixel surface properties and surfaces with greater degrees of anisothermality typically have a greater degree of negative spectral slopes. Importantly, when viewed off-nadir, the resulting change in magnitude of the spectral slopes is diagnostic of the spatial distribution of surface units and their abundance. Using off-nadir data sets provides an independent way to validate rock abundance modeling that previously relied only on nadir data. Moreover, the off-nadir data may provide more accurate values by detecting the sides of rocks not as heavily mantled by dust as the upper surfaces imaged by nadir observations.

Although high-resolution visible images directly identify surface rock abundance, THEMIS TIR data provide greater spatial coverage and a quantitative way to extract thermophysical differences from orbital data (Bandfield, 2009; Bandfield & Edwards, 2008; Cowart & Rogers, 2021). For example, the surfaces observed in proximity to Apollinaris Mons show highly variable spectral slopes. Spectral slope modeling at each viewing angle indicates an increasing derived rock abundance, with the maximum and minimum viewing angles ( $-31^\circ$  and  $0^\circ$ ) providing endmember estimates.

Relative rock abundance models do not provide a comprehensive characterization of surface properties. However, in conjunction with high-resolution visible image data and knowledge of the TI and BT of the surface, they do provide a means to deduce regolith properties such as particle size, compaction/cementation, and surface units (Christensen, 1986). Utilizing the instrument pointing capabilities and higher spatial resolution of THEMIS, we estimate a local rock abundance approaching  $30\% \pm 5\%$  compared to  $3\%–5\%$  derived from previous models using nadir viewing geometries (Christensen, 1986; Nowicki & Christensen, 2007). The effectiveness of this new model results from the off-nadir viewing geometry. Rocks mantled by optically thick surface dust, as thin as a few hundred microns, experience a reduction in TI, and coatings of dust  $\sim 1$  cm in thickness can completely mask the rock signature. Where viewed from nadir these surfaces do not contribute to the emitted radiance (Putzig & Mellon, 2007). However, off-nadir viewing detects the less dust-covered sides of rocks, effectively revealing high TI targets in an otherwise dusty landscape.

Where atmospheric temperatures exceed surface temperatures, traditional THEMIS IR atmospheric correction is not possible. However, in cases where surface emissivity cannot be extracted due to complexities in surface/atmosphere temperature interactions, a two-point BT comparison provides a valid alternative, albeit at a decreased precision. Brightness temperature modeling at study area 2 indicates a complex surface containing a mixture of dust and duricrust-like material in a 75/25 distribution (Table 4) and is supported by CTX data showing abun-

dant small impact craters. These results and the relatively low TI suggest a heavily dust-covered surface with enough cementation to support crater retention, providing insight into the geologic nature of the volcanic fan unit (Figure 12). The derived TI values support prior hypotheses of an underlying volcanoclastic unit mantled by surface dust (Chuang et al., 2019). Additionally, spectral slope modeling may indicate impact gardening by small impacts (crater diameters < 11 m) into the unit.

Unlike study area 1, BT differences are greatest at the nadir viewing geometry (ROTO  $-2$ ,  $+8$ ; Figure 4, Table 4) with more isothermal conditions at higher emission angles. This anisothermal variation indicates that the observed temperature mixing is solely a function of the surface's thermophysical properties and not a result of viewing geometry. Furthermore, it demonstrates the effectiveness of THEMIS ROTO acquisitions in detecting sub-pixel temperature differences from overpasses collected in a relatively short time, compared to using nadir images acquired across multiple local solar times and seasons.

The derived rock abundance estimates enabled by the ROTO measurements are six times greater than previous rock abundance estimates using nadir TIR data. This is due to the fact that off-nadir viewing provides measurements of surfaces not prone to airfall dust cover. This is significant in improving the accuracy of thermophysical and compositional studies. Additionally, the sensitivity of the TIR data is an order of magnitude improvement in scale over radar and visible imaging of the surface. Finally, the unique aspect of ROTOs provide a novel opportunity to re-interpret a surface, revealing previously undetected features at fine scales. This not only aids in geologic interpretation but can provide the groundwork for future exploration.

### Data Availability Statement

This work includes data from multiple instruments spread across various sources and modeling code and results. All THEMIS can be found on the appropriate Data Node under the Planetary Data System (<http://viewer.mars.asu.edu/viewer/themis%23T%3D0>) by searching for the image ID numbers (I86177001, I86202001, I85939006, I85964009, I85989005, I86014012, I86039007, and I86064009). MRO CTX and HiRISE images are available from the Mars Orbital Data Explorer (<https://ode.rsl.wustl.edu/mars/index.aspx>) under the Planetary Data System Geosciences Node by searching for the image ID numbers (B05\_011653\_1714\_XN\_08S186W and ESP\_047230\_178). The KRC thermal model (V 3.5.6) is freely available from Arizona State University and can be found at <http://krc.mars.asu.edu> with detailed instructions on how to download, install, and run the model. The Davinci interface for spectral processing and KRC can be downloaded from <http://davinci.asu.edu>. Spectral Libraries used in the modeling and atmospheric correction as well as all raw results from the KRC model and image data are available in the repository (McKeeby et al., 2022).

### Acknowledgments

The authors would like to recognize Josh Bandfield, who directly influenced the work presented here. Thank you to Deanne Rogers, Vicky Hamilton, Kimm Murray, Jeff Plaut, and Jonathan Hill, who provided direction and guidance on THEMIS TIR image data corrections. Deanne Rogers and an anonymous reviewer provided a formal, constructive, and helpful review that improved the manuscript. Thank you to the members of the THEMIS off-nadir working group whose hard work and planning acquired the ROTO data. Lastly, thank you to Ian Flynn, who provided informal review and feedback to improve the content and clarity of the document. This work was supported by the NASA Mars Odyssey Project and Participating Scientist Program awarded to MSR.

### References

- Ahern, A. A., Rogers, A. D., Edwards, C. S., & Piqueux, S. (2021). Thermophysical properties and surface heterogeneity of landing sites on Mars from overlapping Thermal Emission Imaging System (THEMIS) observations. *Journal of Geophysical Research: Planets*, 126(6), e2020JE006713. <https://doi.org/10.1029/2020je006713>
- Armstrong, J. C., Titus, T. N., & Kieffer, H. H. (2005). Evidence for subsurface water ice in Korolev crater, Mars. *Icarus*, 174(2), 360–372. <https://doi.org/10.1016/j.icarus.2004.10.032>
- Audouard, J., Poulet, F., Vincendon, M., Bibring, J. P., Forget, F., Langevin, Y., & Gondet, B. (2014). Mars surface thermal inertia and heterogeneities from OMEGA/MEX. *Icarus*, 233, 194–213. <https://doi.org/10.1016/j.icarus.2014.01.045>
- Bandfield, J. L. (2006). Extended surface exposures of granitoid compositions in Syrtis Major, Mars. *Geophysical Research Letters*, 33(6), L06203. <https://doi.org/10.1029/2005gl025559>
- Bandfield, J. L. (2008). High-silica deposits of an aqueous origin in Western Hellas Basin, Mars. *Geophysical Research Letters*, 35(12), L12205. <https://doi.org/10.1029/2008gl033807>
- Bandfield, J. L. (2009). Effects of surface roughness and graybody emissivity on martian thermal infrared spectra. *Icarus*, 202(2), 414–428. <https://doi.org/10.1016/j.icarus.2009.03.031>
- Bandfield, J. L., & Edwards, C. S. (2008). Derivation of Martian surface slope characteristics from directional thermal infrared radiometry. *Icarus*, 193(1), 139–157. <https://doi.org/10.1016/j.icarus.2007.08.028>
- Bandfield, J. L., & Feldman, W. C. (2008). Martian high latitude permafrost depth and surface cover thermal inertia distributions. *Journal of Geophysical Research*, 113(E8), E08001. <https://doi.org/10.1029/2007je003007>
- Bandfield, J. L., Hayne, P. O., Williams, J.-P., Greenhagen, B. T., & Paige, D. A. (2015). Lunar surface roughness derived from LRO Diviner Radiometer observations. *Icarus*, 248, 357–372. <https://doi.org/10.1016/j.icarus.2014.11.009>
- Bandfield, J. L., Piqueux, S., Glotch, T. D., Shirley, K. A., Duxbury, T. C., Hill, J. R., et al. (2018). Mars Odyssey THEMIS observations of phobos: New spectral and thermophysical measurements. In *49th annual lunar and planetary science conference* (No. (2083), p. 2643).
- Bandfield, J. L., Rogers, D., Smith, M. D., & Christensen, P. R. (2004). Atmospheric correction and surface spectral unit mapping using Thermal Emission Imaging System data. *Journal of Geophysical Research*, 109(E10), E10008. <https://doi.org/10.1029/2004JE002289>

- Bandfield, J. L., & Smith, M. D. (2003). Multiple emission angle surface–atmosphere separations of Thermal Emission Spectrometer data. *Icarus*, 161(1), 47–65. [https://doi.org/10.1016/s0019-1035\(02\)00025-8](https://doi.org/10.1016/s0019-1035(02)00025-8)
- Beddingfield, C. B., Moersch, J. E., & McSween, H. Y., Jr. (2018). Investigating crater rim thermal inertia variations on Mars: A case study in Tisia Valles. *Icarus*, 314, 345–363. <https://doi.org/10.1016/j.icarus.2018.06.011>
- Beddingfield, C. B., Moersch, J. E., & McSween, H. Y., Jr. (2021). The relationship between thermal inertia and degradation state of craters in areas of low surface dust cover on Mars. *Icarus*, 370, 114678. <https://doi.org/10.1016/j.icarus.2021.114678>
- Bradley, B. A., Sakimoto, S. E., Frey, H., & Zimbelman, J. R. (2002). Medusae Fossae formation: New perspectives from Mars global surveyor. *Journal of Geophysical Research*, 107(E8), 2–1. <https://doi.org/10.1029/2001je001537>
- Chase, S. C., Engel, J. L., Eyerly, H. W., Kieffer, H. H., Palluconi, F. D., & Schofield, D. (1978). Viking infrared thermal mapper. *Applied Optics*, 17(8), 1243–1251. <https://doi.org/10.1364/ao.17.001243>
- Chase, S. C., Miner, E. D., Morrison, D., Mnch, G., Neugebauer, G., & Schroeder, M. (1974). Preliminary infrared radiometry of the night side of Mercury from Mariner 10. *Science*, 185(4146), 142–145. <https://doi.org/10.1126/science.185.4146.142>
- Christensen, P. R. (1986). The spatial distribution of rocks on Mars. *Icarus*, 68(2), 217–238. [https://doi.org/10.1016/0019-1035\(86\)90020-5](https://doi.org/10.1016/0019-1035(86)90020-5)
- Christensen, P. R., Bandfield, J. L., Bell, J. F., III, Gorelick, N., Hamilton, V. E., Ivanov, A., et al. (2003). Morphology and composition of the surface of Mars: Mars Odyssey THEMIS results. *Science*, 300(5628), 2056–2061. <https://doi.org/10.1126/science.1080885>
- Christensen, P. R., Bandfield, J. L., Hamilton, V. E., Howard, D. A., Lane, M. D., Piatek, J. L., et al. (2000). A thermal emission spectral library of rock-forming minerals. *Journal of Geophysical Research*, 105(E4), 9735–9739. <https://doi.org/10.1029/1998je000624>
- Christensen, P. R., Jakosky, B. M., Kieffer, H. H., Malin, M. C., McSween, H. Y., Nealon, K., et al. (2004). The Thermal Emission Imaging System (THEMIS) for the Mars 2001 Odyssey Mission. *Space Science Reviews*, 110(1), 85–130. <https://doi.org/10.1023/b:spac.0000021008.16305.94>
- Chuang, F. C., Crown, D. A., & Berman, D. C. (2019). Geology of the northeastern flank of Apollinaris Mons, Mars: Constraints on the erosional history from morphology, topography, and crater populations. *Icarus*, 333, 385–403. <https://doi.org/10.1016/j.icarus.2019.06.008>
- Cowart, J. C., & Rogers, A. D. (2021). Investigating sources of spectral olivine Enrichments in Martian bedrock plains using diurnal emissivity changes in THEMIS multispectral images. *Journal of Geophysical Research: Planets*, 126(11), e2021JE006947. <https://doi.org/10.1029/2021je006947>
- Crown, D. A., & Ramsey, M. S. (2017). Morphologic and thermophysical characteristics of lava flows southwest of Arsia Mons, Mars. *Journal of Volcanology and Geothermal Research*, 342, 13–28. <https://doi.org/10.1016/j.jvolgeores.2016.07.008>
- Davidsson, B. J., Rickman, H., Bandfield, J. L., Groussin, O., Gutiérrez, P. J., Wilska, M., et al. (2015). Interpretation of thermal emission. I. The effect of roughness for spatially resolved atmosphereless bodies. *Icarus*, 252, 1–21. <https://doi.org/10.1016/j.icarus.2014.12.029>
- Dollfus, A., & Deschamps, M. (1986). Grain-size determination at the surface of Mars. *Icarus*, 67(1), 37–50. [https://doi.org/10.1016/0019-1035\(86\)90172-7](https://doi.org/10.1016/0019-1035(86)90172-7)
- Edgett, K. S., Butler, B. J., Zimbelman, J. R., & Hamilton, V. E. (1997). Geologic context of the Mars radar “Stealth” region in southwestern Tharsis. *Journal of Geophysical Research*, 102(E9), 21545–21567. <https://doi.org/10.1029/97je01685>
- Edwards, C. S., Bandfield, J. L., Christensen, P. R., & Fergason, R. L. (2009). Global distribution of bedrock exposures on Mars using THEMIS high-resolution thermal inertia. *Journal of Geophysical Research*, 114(E11), E11001. <https://doi.org/10.1029/2009je003363>
- Edwards, C. S., Piqueux, S., Hamilton, V. E., Fergason, R. L., Herkenhoff, K. E., Vasavada, A. R., et al. (2018). The thermophysical properties of the Bagnold Dunes, Mars: Ground-truthing orbital data. *Journal of Geophysical Research: Planets*, 123(5), 1307–1326. <https://doi.org/10.1029/2017je005501>
- El Maarry, M. R., Dohm, J. M., Marzo, G. A., Fergason, R., Goetz, W., Heggy, E., et al. (2012). Searching for evidence of hydrothermal activity at Apollinaris Mons, Mars. *Icarus*, 217(1), 297–314. <https://doi.org/10.1016/j.icarus.2011.10.022>
- El-Maarry, M. R., Heggy, E., & Dohm, J. M. (2014). Radar investigations of Apollinaris Mons on Mars: Exploring the origin of the fan deposits. *Planetary and Space Science*, 103, 262–272. <https://doi.org/10.1016/j.pss.2014.09.007>
- Farrell, A. K., & Lang, N. P. (2010). Distribution of explosive and effusive volcanic deposits at Apollinaris Patera, Mars. In *41st annual lunar and planetary science conference* (No. (1533), p. 2072).
- Fenton, L. K., Bandfield, J. L., & Ward, A. W. (2003). Aeolian processes in Proctor Crater on Mars: Sedimentary history as analyzed from multiple data sets. *Journal of Geophysical Research*, 108(E12), 5129. <https://doi.org/10.1029/2002je002015>
- Fergason, R. L. (2014). *Thermal inertia mosaic quantitative map from 30°S to 240°E*. USGS Astrogeology Science Center.
- Fergason, R. L., Christensen, P. R., & Kieffer, H. H. (2006). High-resolution thermal inertia derived from the Thermal Emission Imaging System (THEMIS): Thermal model and applications. *Journal of Geophysical Research*, 111(E12), E12004. <https://doi.org/10.1029/2006JE002735>
- Gillespie, A. R., Kahle, A. B., & Walker, R. E. (1986). Color enhancement of highly correlated images: I. Decorrelation and HIS contrast stretches. *Remote Sensing of Environment*, 20(3), 209–235. [https://doi.org/10.1016/0034-4257\(86\)90044-1](https://doi.org/10.1016/0034-4257(86)90044-1)
- Golombek, M. P., Haldemann, A. F. C., Forsberg-Taylor, N. K., DiMaggio, E. N., Schroeder, R. D., Jakosky, B. M., et al. (2003). Rock size-frequency distributions on Mars and implications for Mars Exploration Rover landing safety and operations. *Journal of Geophysical Research: Planets*, 108(E12). <https://doi.org/10.1029/2002je002035>
- Greeley, R., & Spudis, P. D. (1981). Volcanism on Mars. *Reviews of Geophysics*, 19(1), 13–41. <https://doi.org/10.1029/rg019i001p00013>
- Gregg, T. K. P., & Krysak, D. J. (2011). Apollinaris Mons, Mars: A new name and a new past. In *42nd annual lunar and planetary science conference* (No. (1608), p. 1922).
- Gulick, V. C., & Baker, V. R. (1990). Origin and evolution of valleys on Martian volcanoes. *Journal of Geophysical Research*, 95(B9), 14325–14344. <https://doi.org/10.1029/jb095ib09p14325>
- Hamilton, V. E., & Christensen, P. R. (2005). Evidence for extensive, olivine-rich bedrock on Mars. *Geology*, 33(6), 433–436. <https://doi.org/10.1130/g21258.1>
- Hayne, P. O., Bandfield, J. L., Siegler, M. A., Vasavada, A. R., Ghent, R. R., Williams, J. P., et al. (2017). Global regolith thermophysical properties of the moon from the diviner lunar radiometer experiment. *Journal of Geophysical Research: Planets*, 122(12), 2371–2400. <https://doi.org/10.1002/2017je005387>
- Hiesinger, H., Helbert, J., Alemanno, G., Bauch, K. E., D’Amore, M., Maturilli, A., et al. (2020). Studying the composition and mineralogy of the hermean surface with the Mercury radiometer and thermal infrared spectrometer (MERTIS) for the BepiColombo mission: An update. *Space Science Reviews*, 216(6), 1–37. <https://doi.org/10.1007/s11214-020-00732-4>
- Hynek, B. M., Phillips, R. J., & Arvidson, R. E. (2003). Explosive volcanism in the Tharsis region: Global evidence in the Martian geologic record. *Journal of Geophysical Research*, 108(E9), 5111. <https://doi.org/10.1029/2003je002062>
- Jakosky, B. M. (1978). Modeling of the Martian surface: Thermal inertia and related characteristics. In *Lunar and planetary science conference* (Vol. 9, pp. 579–581).
- Jakosky, B. M. (1986). On the thermal properties of Martian fines. *Icarus*, 66(1), 117–124. [https://doi.org/10.1016/0019-1035\(86\)90011-4](https://doi.org/10.1016/0019-1035(86)90011-4)

- Kieffer, H. H. (2013). Thermal model for analysis of Mars infrared mapping. *Journal of Geophysical Research: Planets*, 118(3), 451–470. <https://doi.org/10.1029/2012je004164>
- Kieffer, H. H., Christensen, P. R., & Titus, T. N. (2006). CO<sub>2</sub> jets formed by sublimation beneath translucent slab ice in Mars' seasonal south polar ice cap. *Nature*, 442(7104), 793–796. <https://doi.org/10.1038/nature04945>
- Kieffer, H. H., Martin, T. Z., Peterfreund, A. R., Jakosky, B. M., Miner, E. D., & Palluconi, F. D. (1977). Thermal and albedo mapping of Mars during the Viking primary mission. *Journal of Geophysical Research*, 82(28), 4249–4291. <https://doi.org/10.1029/JS082i028p04249>
- Lane, M. D., & Christensen, P. R. (1998). Thermal infrared emission spectroscopy of salt minerals predicted for Mars. *Icarus*, 135(2), 528–536. <https://doi.org/10.1006/icar.1998.5998>
- Lang, N. P., McSween, H. Y., Jr., Tornabene, L. L., Hardgrove, C. J., & Christensen, P. R. (2010). Reexamining the relationship between Apollinaris Patera and the basalts of the Gusev crater plains, Mars. *Journal of Geophysical Research*, 115(E4), E04006. <https://doi.org/10.1029/2009je003397>
- Mandt, K. E., de Silva, S. L., Zimbelman, J. R., & Crown, D. A. (2008). Origin of the Medusae Fossae formation, Mars: Insights from a synoptic approach. *Journal of Geophysical Research*, 113(E12), E12011. <https://doi.org/10.1029/2008je003076>
- McColley, S. M., Head, J. W., & Neukum, G. (2005). The Medusae Fossae Formation: Geological characteristics and topographic and stratigraphic relationships of the lower member along southeastern Elysium Planitia (abstract). In *Proceedings of the Lunar and Planetary Science Conference* (Vol. 36, p. 1184).
- McKeeby, B. E., & Ramsey, M. S. (2020). Spectral anisothermality: A two-look approach to thermal infrared data analysis of planetary basaltic surfaces. In *51st lunar planetary science conference*. abs. #2083.
- McKeeby, B. E., & Ramsey, M. S. (2021). Deriving planetary surface roughness: Combining digital photogrammetry and thermal infrared spectroscopy. In *52nd lunar planetary science conference*. abs. #1957.
- McKeeby, B. E., Ramsey, M. S., Udovicic, C. T., Haberle, C., & Edwards, C. S., (2022). Apollinaris Mons [Dataset]. Zenodo. <https://doi.org/10.5281/zenodo.6522670>
- Mellon, M. T., Jakosky, B. M., Kieffer, H. H., & Christensen, P. R. (2000). High-resolution thermal inertia mapping from the Mars global surveyor thermal emission spectrometer. *Icarus*, 148(2), 437–455. <https://doi.org/10.1006/icar.2000.6503>
- Mellon, M. T., & Putzig, N. E. (2007). The apparent thermal inertia of layered surfaces on Mars. In *Lunar and planetary science conference* (No. (1338)).
- Montabone, L., Spiga, A., Kass, D. M., Kleinbohl, A., Forget, F., & Millour, E. (2020). Martian year 34 column dust climatology from Mars climate sounder observations: Reconstructed maps and model simulations. *Journal of Geophysical Research: Planets*, 125(8), e2019JE006111. <https://doi.org/10.1029/2019je006111>
- Morrison, D. (1970). Thermophysics of the planet Mercury. *Space Science Reviews*, 11(2), 271–307. <https://doi.org/10.1007/bf00241524>
- Nowicki, S. A., & Christensen, P. R. (2007). Rock abundance on Mars from the thermal emission spectrometer. *Journal of Geophysical Research*, 112(E5), E05007. <https://doi.org/10.1029/2006je002798>
- Osterloo, M. M., Hamilton, V. E., Bandfield, J. L., Glotch, T. D., Baldrige, A. M., Christensen, P. R., et al. (2008). Chloride-bearing materials in the southern highlands of Mars. *Science*, 319(5870), 1651–1654. <https://doi.org/10.1126/science.1150690>
- Piqueux, S., & Christensen, P. R. (2011). Temperature-dependent thermal inertia of homogeneous Martian regolith. *Journal of Geophysical Research*, 116(E7), E07004. <https://doi.org/10.1029/2011je003805>
- Presley, M. A., & Christensen, P. R. (1997). The effect of bulk density and particle size sorting on the thermal conductivity of particulate materials under Martian atmospheric pressures. *Journal of Geophysical Research*, 102(E4), 9221–9229. <https://doi.org/10.1029/97je00271>
- Putzig, N. E., & Mellon, M. T. (2007). Apparent thermal inertia and the surface heterogeneity of Mars. *Icarus*, 191(1), 68–94. <https://doi.org/10.1016/j.icarus.2007.05.013>
- Putzig, N. E., Mellon, M. T., Kretke, K. A., & Arvidson, R. E. (2005). Global thermal inertia and surface properties of Mars from the MGS mapping mission. *Icarus*, 173(2), 325–341. <https://doi.org/10.1016/j.icarus.2004.08.017>
- Ramsey, M. S., & Christensen, P. R. (1998). Mineral abundance determination: Quantitative deconvolution of thermal emission spectra. *Journal of Geophysical Research*, 103(B1), 577–596. <https://doi.org/10.1029/97jb02784>
- Robinson, M. S., Mouginiis-Mark, P. J., Zimbelman, J. R., Wu, S. S., Ablin, K. K., & Howington-Kraus, A. E. (1993). Chronology, eruption duration, and atmospheric contribution of the Martian volcano Apollinaris Patera. *Icarus*, 104(2), 301–323. <https://doi.org/10.1006/icar.1993.1103>
- Rogers, A. D., Christensen, P. R., & Bandfield, J. L. (2005). Compositional heterogeneity of the ancient Martian crust: Analysis of Ares Vallis bedrock with THEMIS and TES data. *Journal of Geophysical Research*, 110(E5), E05010. <https://doi.org/10.1029/2005je002399>
- Rose, S. R., Watson, W., Ramsey, M. S., & Hughes, C. G. (2014). Thermal deconvolution: Accurate retrieval of multispectral infrared emissivity from thermally-mixed volcanic surfaces. *Remote Sensing of Environment*, 140, 690–703. <https://doi.org/10.1016/j.rse.2013.10.009>
- Rubanenko, L., Schorghofer, N., Greenhagen, B. T., & Paige, D. A. (2020). Equilibrium temperatures and directional emissivity of sunlit airless surfaces with applications to the Moon. *Journal of Geophysical Research: Planets*, 125(6), e2020JE006377. <https://doi.org/10.1029/2020je006377>
- Ruff, S. W., & Christensen, P. R. (2002). Bright and dark regions on Mars: Particle size and mineralogical characteristics based on Thermal Emission Spectrometer data. *Journal of Geophysical Research*, 107(E12), 5119, 2–1. <https://doi.org/10.1029/2001je001580>
- Ruff, S. W., Christensen, P. R., Barbera, P. W., & Anderson, D. L. (1997). Quantitative thermal emission spectroscopy of minerals: A laboratory technique for measurement and calibration. *Journal of Geophysical Research*, 102(B7), 14899–14913. <https://doi.org/10.1029/97jb00593>
- Scott, D. H., Dohm, J. M., & Applebee, D. J. (1993). *Geologic map of science study area 8, Apollinaris Patera region of Mars*. US Geological Survey Report. 2351.
- Scott, D. H., & Tanaka, K. L. (1982). Ignimbrites of Amazonis Planitia region of Mars. *Journal of Geophysical Research*, 87(B2), 1179–1190. <https://doi.org/10.1029/JB087iB02p01179>
- Simurda, C. M., Ramsey, M. S., & Crown, D. A. (2019). The unusual thermophysical and surface properties of the Daedalia Planum lava flows. *Journal of Geophysical Research: Planets*, 124(7), 1945–1959. <https://doi.org/10.1029/2018je005887>
- Smith, M. D., Bandfield, J. L., & Christensen, P. R. (2000). Separation of atmospheric and surface spectral features in Mars global surveyor thermal emission spectrometer (TES) spectra. *Journal of Geophysical Research*, 105(E4), 9589–9607. <https://doi.org/10.1029/1999je001105>
- Smith, M. D., Bandfield, J. L., Christensen, P. R., & Richardson, M. I. (2003). Thermal Emission Imaging System (THEMIS) infrared observations of atmospheric dust and water ice cloud optical depth. *Journal of Geophysical Research*, 108(E11), 5115. <https://doi.org/10.1029/2003JE002115>
- Smith, N. M., Edwards, C. S., Mommert, M., Trilling, D. E., & Glotch, T. D. (2018). Mapping the thermal inertia of Phobos using MGS-TES observations and thermophysical modeling. In *49th annual lunar and planetary science conference* (No. (2083), p. 2809).
- Tanaka, K. L. (2000). Dust and ice deposition in the Martian geologic record. *Icarus*, 144(2), 254–266. <https://doi.org/10.1006/icar.1999.6297>
- Titus, T. N., Kieffer, H. H., & Christensen, P. R. (2003). Exposed water ice discovered near the south pole of Mars. *Science*, 299(5609), 1048–1051. <https://doi.org/10.1126/science.1080497>

- Vasavada, A. R., Bandfield, J. L., Greenhagen, B. T., Hayne, P. O., Siegler, M. A., Williams, J. P., & Paige, D. A. (2012). Lunar equatorial surface temperatures and regolith properties from the Diviner Lunar Radiometer Experiment. *Journal of Geophysical Research*, *117*(E12), E00H18. <https://doi.org/10.1029/2011je003987>
- Warren, T. J., Bowles, N. E., Donaldson Hanna, K., & Bandfield, J. L. (2019). Modeling the angular dependence of emissivity of randomly rough surfaces. *Journal of Geophysical Research: Planets*, *124*(2), 585–601. <https://doi.org/10.1029/2018je005840>
- Williams, J. P., Paige, D. A., Greenhagen, B. T., & Sefton-Nash, E. (2017). The global surface temperatures of the moon as measured by the diviner lunar radiometer experiment. *Icarus*, *283*, 300–325. <https://doi.org/10.1016/j.icarus.2016.08.012>
- Zimbelman, J. R., & Griffin, L. J. (2010). HiRISE images of yardangs and sinuous ridges in the lower member of the Medusae Fossae Formation, Mars. *Icarus*, *205*(1), 198–210. <https://doi.org/10.1016/j.icarus.2009.04.003>